Assessing landscape and seasonal controls on CO_2 fluxes in a karst sinkhole

Taryn Karie Thompson

Thesis submitted to the faculty of the Virginia Polytechnic Institute and State University in partial fulfillment of the requirements for the degree of

Master of Science
In
Crop and Soil Environmental Sciences

Ryan Stewart
Daniel McLaughlin
Madeline Schreiber

September 22, 2021
Blacksburg, Virginia

Keywords: concentration gradient, zero-flux plane, gradient method, diffusion coefficient, Fick's Law

Assessing landscape and seasonal controls on CO_2 fluxes in a karst sinkhole

Taryn Karie Thompson

SCIENTIFIC ABSTRACT

Karst landscapes can serve as carbon sinks when carbon dioxide (CO_2) reacts with water to form carbonic acid, which then weathers carbonate rocks. However, CO_2 can also move through the subsurface via gas diffusion, a process that is not well-understood in karst systems. This study focused on quantifying CO_2 diffusion within a karst sinkhole. The objectives of this study were to: 1) identify the depth of the zero-flux plane (i.e., depths of local maximum CO_2 concentrations), analyze the distributions of concentration gradients, and investigate the validity of a uniform concentration gradient throughout the profile; and 2) assess the influences of vertical position and seasonality on CO_2 fluxes within this sinkhole. The study site contained three locations within the sinkhole, including shoulder, backslope, and toeslope locations. Each location had three soil CO_2 and three soil water content/temperature sensors placed at 20, 40, and 60 cm depths. Zero-flux planes were seldom detectable during the warm season (April-September) but were frequently found near the surface (20 or 40 cm) during the cool season (October-March). The common assumption of a uniform concentration gradient was often invalid based on relative concentrations between sensor pairs. As for the second objective, CO_2 fluxes generally followed a trend of upward fluxes in warmer months that was partially offset by downward fluxes during the cooler months. These study results provide new insight into CO_2 dynamics in a karst system, and suggest that subsurface processes such as chemical weathering and cave ventilation affect the direction and magnitude of CO_2 fluxes.

PUBLIC ABSTRACT

Carbon dioxide (CO_2) within soils is a larger pool of CO_2 than atmospheric CO_2. Therefore, the movement of CO_2 within soils is important to understand, as soil CO_2 may eventually diffuse through the soil and into the atmosphere. Soil CO_2 movement is dependent on many factors such as soil water content, porosity, and temperature. Soil CO_2 movement may vary between landscapes as well, due to chemical weathering processes being sinks of soil and atmospheric CO_2. One type of important landscape is karst, which can be identified by easily soluble rocks, usually in the forms of limestone and dolomite rocks. In order to investigate the influences of karst landscapes on the movement of soil CO_2, in this study I identified the depths of CO_2 maximum concentrations and CO_2 movement over time and by sinkhole slope position. The results from this study were that the depth of maximum CO_2 concentration was deeper, > 40 cm, during the warmer months and often shallower, ≤ 40 cm, during the cooler months. The CO_2 fluxes generally followed a trend of upward fluxes in warmer months that was partially offset by downward fluxes during the cooler months. The results from this study suggest that due to vertical differences in soil properties, temperature, chemical weathering of the karst rock, and cave ventilation the depth of the maximum CO_2 concentration and the CO_2 movement vary by season and sinkhole slope location. This study provides new insight to CO_2 movement relative to karst landscapes while highlighting the importance of soil and geologic properties as influences that can alter the direction and magnitude of CO_2 fluxes.

ACKNOWLEDGEMENT

I would like to acknowledge several people, without whom the completion of this thesis would not have been possible.

I recognize my advisor, Dr. Ryan Stewart, as he has helped me grow as a student and professional, thanks to his knowledge and guidance. His investment in this project and my academic success are immeasurable.

I thank my committee members, Dr. Daniel McLaughlin and Dr. Madeline Schreiber, for their time and investment in the creation of this project and thesis content.

I acknowledge my lab group as they have brought fun to this experience. Our weekly lab meetings consisted of camaraderie and a space for creative thinking and professional growth.

I thank the George Washington Carver program for supporting my academic progress through financial support. I appreciate the communal support within this program that stems from shared experiences and celebrates successes within the community. I thank the School of Plant and Environmental Sciences for their financial support throughout this portion of my academic journey, as well.

Finally, I thank my family for their excitement of my everyday accomplishments throughout this program and for their unending support and helpful advice.

Table of Contents

1. Introduction

Carbon dioxide (CO_2) is one of the main types of greenhouse gases within the atmosphere. Soil serves as a major pool of CO_2 within the global carbon cycle (Kutsch et al., 2009; Trivedi et al., 2018; Raich & Potter, 1995; Bond-Lamberty & Thomson, 2010) and can act as a carbon sink when rates of assimilation by production outpace respiration rates (Trivedi et al., 2018). The magnitudes of CO_2 flux from the soil surface into the atmosphere vary based on environmental factors, including, but not limited to, landscape type, vegetation type, season, and soil water content. CO_2 is primarily produced in the subsurface by respiration, including from autotrophs (primarily plants) and from heterotrophs (primarily microbes) (Shi et al., 2012; Brown & Markewitz, 2018). Once produced, CO_2 moves through the subsurface via two main mass transport mechanisms: advection and diffusion, with diffusion typically acting as the more important process (Jin & Jury, 1996; Schjønning et al., 2013; Pumpanen et al., 2003; Laemmel et al., 2017).

Soil gas diffusion is caused by differences in CO_2 concentrations throughout a soil profile and between the soil surface and atmosphere (which now has an average concentration of around 415 parts per million by volume, or ppmv). For a given change in soil CO_2 concentration over distance (i.e., concentration gradient), gas diffusion rates can be estimated using the one-dimensional version of Fick's Law:

$$J = -D_s \frac{\Delta C}{\Delta x} \quad (1)$$

where J is the flux density [N L^{-2} T^{-1}], ΔC is the change in concentration [N L^{-3}] over some distance Δx [L], and D_s [L^2 T^{-1}] is the gas diffusion constant. The gas diffusion coefficient is affected by various physical properties, with the volume of air-filled pores often representing the

most important term (Moldrup et al., 2004; Iiyama & Hasegawa, 2005; Jayarathne et al., 2020). While some field methods exist to quantify D_s (e.g., Allaire et al., 2008; Shcherbak & Philip Robertson, 2014), the parameter is more commonly measured using intact or repacked samples in the laboratory (Iiyama & Hasegawa, 2005; Kristensen et al., 2010).

Recent sensor advances have created the ability to collect high-frequency CO_2 measurements in soil profiles. These measurements have revealed that, in most soil profiles, CO_2 concentrations increase with depth due to greater bulk density (Farmer et al., 1973; Jin & Jury, 1996; Jassal et al., 2005) and lesser porosity (So & Nye, 1989; Fujikawa & Miyazaki, 2005; Jin & Jury, 1996; Jassal et al., 2005) at depth limiting diffusion of CO_2 toward the soil surface. At the same time, soil CO_2 concentrations tend to increase in response to increases in temperatures and available water content, which enhance microbial activity (Benavente et al., 2010). These fluctuations can be manifest on diurnal timescales, with peak concentrations often seen during the afternoon hours (Tang et al., 2003), and on seasonal timescales, with higher concentrations often seen in the warm growing season (e.g., April through September in the mid-latitudes of the Northern Hemisphere; Blecha & Faimon, 2014).

Soil CO_2 concentrations and diffusion rates can also exhibit spatial variation. For example, disturbances such as mechanical tillage can induce a short-term spike in soil respiration, leading to temporary increases in gas concentrations and diffusion rates (Reicosky & Lindstrom, 1993). Soil respiration can also differ along elevation transects, such as along hillslopes, due to differences in vegetation productivity and water availability (Saggar et al., 1999). Further, soil heterogeneity, such as the presence of macropores and other large air-filled spaces, can increase the ability of gas to diffuse through the subsurface (Moldrup et al., 2000; Kristensen et al., 2010). These features are often irregularly distributed across a landscape (Jackisch et al., 2017; Di Prima

et al., 2021), and can change through time as some macropores become filled in with material and new ones develop from biological and physical processes (Beven & Germann, 1982).

The temporal and spatial variability of CO_2 gas diffusion may be even more pronounced in landscapes with karst geology, which occupy as much as 15% of global land surface (Fang et al., 2012). Karst is comprised of soluble carbonate rocks, such as dolomite and limestone, that can undergo relatively rapid weathering when rainwater and carbon dioxide react to form carbonic acid (Eagle et al., 2015). As an example, calcium carbonate ($CaCO_3$) reacts with carbonic acid to form a calcium ion and two bicarbonate ions, HCO_3^-:

$$CaCO_3 + H_2CO_3 \leftrightarrow Ca^{2+} + 2HCO_3^- \quad (2)$$

Even though some of the CO_2 within the bicarbonate ions is released when $CaCO_3$ precipitates out of solution forming speleothems within caves (White, 2016), this dissolution process can serve as a large-scale carbon sink over timescales ranging from thousands to hundreds of thousands of years (Fang et al., 2012). The weathering reaction also creates highly fractured epikarst layers beneath the soil profile and above the karst bedrock and any cave layers (Schreiber et al., 2015).

Crack and fissure networks within epikarst can allow for rapid gas and liquid transport (Eagle et al., 2015). However, most previous research has focused on advective transport (i.e., leaching) and mass movement via cave venting. For example, a study in James Cave in Virginia showed that dissolved CO_2 primarily moved within the cave drip system between November and March, due to seasonal filling and then spilling of the epikarst layer (Eagle et al., 2015). Other studies have revealed that 1) karst caves in temperate climates often experience seasonal fluctuations in CO_2, due to temperature differences between the cave and overlying atmosphere encouraging

venting and gas exchange during colder months (when cave air is often warmer and less dense than the atmosphere), thus decreasing CO_2 concentrations (Krajnc et al., 2017); and 2) higher soil respiration during the spring and summer growing season increasing the partial pressure of CO_2 within soil, which can cause CO_2 to move into epikarst and caves via percolating water (Eagle et al., 2015; Jiang et al., 2020). However, in many karst systems, the epikarst is separated from the atmosphere by a soil mantle, which can act as a buffer against rapid convection-induced mass transport of CO_2 from the cave system to the atmosphere through fissures (Sánchez-Cañete et al., 2016).

The role of soil mantles in regulating gas diffusion in karst systems remains poorly understood, particularly compared to the well-studied CO_2 soil profile patterns in other landscapes (Cueva et al., 2015; Fa et al., 2015; Fan & Jones, 2014; Jassal et al., 2005; Liu et al., 2015; Pingintha et al., 2010; Saggar et al., 1999; Sánchez-Cañete et al., 2017; Turcu et al., 2005; Wolf et al., 2011). In particular, karst systems can have decreasing CO_2 concentrations at depth, due to losses to caves and consumption during carbonate weathering (Cao et al., 2020; White, 2016). In such circumstances, the maximum CO_2 concentration will reside somewhere between the soil surface and the cave, thus forming a zero-flux plane. Above the zero-flux plane, gas will diffuse into the atmosphere, whereas below this point CO_2 could potentially move into epikarst and caves. The existence and relative position of the zero-flux plane therefore represents a potentially important, but largely understudied, control on soil diffusion processes. At the same time, the incidence and magnitude of downward diffusion through karst systems have not been quantified, even though this process may represent an important aspect of CO_2 movement within these systems.

The research project discussed in this thesis aims to understand spatial and temporal changes in CO_2 concentrations in a karst landscape. The thesis is comprised of two main chapters. In the

first part of the study (Chapter 2), I track the relative location of maximum CO_2 concentrations within two soil profiles located above a karst cave system and quantify the proportion of time the zero-flux plane exists above versus below the rooting zone over a one-year period. In the second part of the study (Chapter 3), I identify the direction and magnitude of CO_2 fluxes. I then discuss how sinkhole slope position and seasonal drivers influence the underlying processes. Even though this project is focused on only one site, the findings should be generalizable to other karst systems with similar geologic and environmental factors.

2. Assessing concentration gradients and the zero-flux plane dynamics using multiple soil CO_2 sensors

2.1 Abstract

Soil CO_2 concentrations typically increase with depth as higher bulk densities and lower air-filled porosities cause decreased CO_2 diffusion rates. However, karst landscapes possess subsurface sinks for CO_2, including caves and weathering reactions, which can decrease CO_2 concentrations at depth. These conditions may induce downward CO_2 diffusion, yet the frequency with which this process occurs is not well understood. In this study, solid-state soil CO_2 sensors were installed at depths of 20, 40, and 60 cm at the shoulder and toeslope of a sinkhole slope. The zero-flux plane, i.e., the vertical position where CO_2 flux diverges between upward and downward directions, was identified whenever the 20 or 40 cm sensors measured higher concentrations than deeper sensors. At the same time, the validity of the common assumption of a uniform CO_2 concentration gradient throughout the subsurface was evaluated by comparing 20 to 40 cm, 40 to 60 cm, and 20 to 60 cm sensor pairs. The results indicated that, during the warm growing season months (April-September), zero-flux planes rarely existed near the soil surface, with maximum concentrations existing at 20 or 40 cm only 12% of the time at the shoulder and 16% of the time at the toeslope. During the cool season (October-March), however, near-surface zero-flux planes were detected 37% of the time in the toeslope location. The concentration gradients produced by the three sets of sensor pairs had similar cumulative distributions, though the 20 to 60 cm lacked the extreme positive and negative values of the other pairings. Furthermore, even when concentration gradients were monotonic (i.e., had the same direction) between the 20 to 40 cm and the 40 to 60 cm sensor pairings, the relative gradients measured by each varied by more than an order of magnitude in 6-9% of records. Therefore, the

assumption of a uniform gradient was often invalid within these soil profiles. Altogether, the frequent presence of near-surface zero-flux planes indicates that downward diffusion of CO_2 may be an important process affecting the ability of karst landscapes to serve as CO_2 sinks.

2.2 Introduction

Near-surface soils represent the largest terrestrial pool of carbon (Kutsch et al., 2009) and carbon dioxide (CO_2) efflux from soils into the atmosphere is the second largest terrestrial flux of carbon (Cueva et al., 2015; Bond-Lamberty & Thomson, 2010). The dynamics that regulate soil CO_2 concentrations and emissions vary between landscapes, land uses, climate, and temperature regimes (Wanyama et al., 2019; Raich & Schlesinger, 1992; Risk et al., 2002). At the same time, a multitude of environmental conditions influence CO_2 concentrations, such as carbon allocation, temperature, precipitation or volumetric soil water content, vegetation type and amount, soil structure, porosity, and bulk density (Saggar et al., 1999; Risk et al., 2002; Kiefer, 1990; Kaspar & Parkin, 2011). Therefore, it is important to understand subsurface CO_2 movement within and through heterogeneous soils, particularly in landscapes formed from sedimentary materials, such as carbonate rocks, as the weathering of these materials can influence carbon cycles and function as carbon sinks (Zhao et al., 2021; Schlesinger, 1986; Serrano-Ortiz et al., 2010; Rey, 2015). This information is particularly important for local and regional carbon budgeting and can aid in more accurate quantification of global carbon budgets (Pingintha et al., 2010; Wan et al., 2019; Pumpanen et al., 2003; Cueva et al., 2015).

CO_2 movement within soils is driven by gas diffusion in response to differences in concentration (Hillel, 2003), as soil conditions generally limit advection (Jin & Jury, 1996; Schjønning et al., 2013; Pumpanen et al., 2003; Laemmel et al., 2017). Diffusion is contingent upon CO_2 concentrations, as gases diffuse from areas of high to low concentration (Hillel, 2003). Within a

typical soil profile, CO_2 concentrations tend to increase with depth, as higher bulk densities and lower air-filled porosities typically restrict the rate at which CO_2 can diffuse to the surface (Benavente et al., 2010; Tang et al., 2003; Chen, 2019). However, this pattern may vary between different landscape types.

Several studies performed in karst landscapes, which contain sedimentary rock formations comprised of soluble dolomite and limestone, have reported relatively low CO_2 concentrations within soil and epikarst layers (Chen, 2019; Krajnc et al., 2017; Blecha & Faimon, 2014; Zhao et al., 2019; Benavente et al., 2010; Crowther, 1984). One explanation for this behavior is that CO_2 is consumed during the formation of carbonic acid and subsequent weathering of calcium carbonate rock (Fang et al., 2012). Another explanation is that the subsurface venting of cave air removes CO_2 from soil and epikarst, as Benavente et al. (2010) showing that 30-50% of CO_2 in a Mediterranean cave originated from the overlying soil profile. This venting process can occur whenever cave air is warmer, and more buoyant, than the air outside the cave (Krajnc et al., 2017; Mattey et al., 2016). Nonetheless, limited observational data have been collected to validate and understand CO_2 concentrations within karst soils.

Soil CO_2 diffusion rates are typically measured using one of two methods: 1) a flux chamber placed on the soil surface that estimates soil CO_2 efflux from the change of gas concentrations within the chamber (Wolf et al., 2011), or 2) a gradient-based method that estimates gas diffusion rates using CO_2 concentrations measured by sensors installed at two or more depths in the subsurface (Tang et al., 2003). Chamber measurements are widely used due to their accuracy in measuring CO_2 efflux from the soil surface (Wolf et al., 2011); the ease with which they are deployed (Sánchez-Cañete et al., 2017; Peng et al., 2012); and their ability to render accurate measurements (Turcu et al., 2005; Peng et al., 2012). However, chambers alter the environmental

conditions of the surface by disturbing vegetation, buffering air pressure changes due to wind (Laemmel et al., 2017; Tang et al., 2003), and preventing precipitation from reaching the soil surface (Laemmel et al., 2017; Tang et al., 2003). The chamber method is also limited in temporal-scope as it is difficult to maintain chambers over long periods (Luther-Mosebach et al., 2018). In contrast, the gradient method typically uses solid-state CO_2 sensors that are installed at fixed depths and record near-continuous concentration readings. After installation of the sensors, there is no further soil disturbance and the solid-state CO_2 sensors are less impacted by environmental conditions. In addition, solid-state CO_2 sensors have the ability to estimate downward fluxes, as opposed to surface chamber systems that exclusively measure upward efflux. The ability of solid-state CO_2 sensors to estimate downward flux is vitally important in systems with potential CO_2 sinks at depth, such as can exist in karst terrain.

Many studies have utilized the gradient method to calculate CO_2 fluxes (Cueva et al., 2015; Tang et al., 2003; Yang et al., 2018; Jassal et al., 2005; Maier & Schack-Kirchner, 2014; Vargas et al., 2010; Turcu et al., 2005; Fan & Jones, 2014; Pingintha et al., 2010; Pumpanen et al., 2003; Xiao et al., 2015; Jong & Schappert, 1972). Some of these studies have calculated a mean CO_2 concentration gradient via linear regression between measured CO_2 concentrations at different depths (Tang et al., 2003; Yang et al., 2018). However, Cueva et al. (2015) noted variance in CO_2 efflux when assuming a uniform concentration gradient within the soil profile versus the measured concentration gradient between a shallow soil depth and the atmosphere. Similarly, increased amounts of respiration near the soil surface (< 10 cm) can contribute more to total efflux than deeper layers (Luther-Mosebach et al., 2018). These results support the notion that it might not be appropriate to assume a uniform concentration gradient across depths within many

soil profiles. Yet, few studies have investigated the effects of relative sensor depths on the calculated flux using the gradient method.

The assumption of a uniform CO_2 gradient may be even more problematic in karst soils, where the subsurface CO_2 sinks could create zero-flux CO_2 planes, i.e., depths in the subsurface at which vertical fluxes either diverge or converge. Zero-flux planes would occur whenever there is a local minimum or maximum of CO_2 concentration, with the former associated with converging diffusive fluxes and the latter associated with diverging fluxes. Previously, zero-flux planes have been considered in the context of water movement through the vadose zone (Brutsaert, 2014; Khalil et al., 2003; Villegas & Morris, 1990), but the concept has not been explored in terms of soil gas fluxes. Therefore, there is a need to study both existence of zero-flux planes and their influence on subsurface CO_2 movement.

In this study, I sought to investigate spatial and temporal variations in CO_2 concentrations in two soil profiles above a karst cave system. Both profiles were located in a sinkhole, one at the shoulder and the other profile at the toeslope. In each soil profile, I used CO_2 concentration measurements from sensors installed at 20, 40, and 60 cm depths. The duration of the study was from 1 April 2017 through 31 March 2018. My first objective was to identify the existence and calculate the frequency of the zero-flux plane within the uppermost 40 cm of the soil profiles. My second objective was to evaluate how the concentration gradients varied between the sensor pairs, 20 cm and 40 cm, 40 cm and 60 cm, and 20 cm and 60 cm. My third objective was to compare the concentration gradients between sensor pairs in order to determine how frequently a uniform concentration gradient existed within the soil profiles.

2.3 Methods

2.3.1 Site description and instrumentation

James Cave is a doline karst cave located in southwest Virginia, U.S. (Eagle et al., 2015). The cave entrance is located at the toeslope of a sinkhole on a cattle farm. The main vegetation type is tall fescue grass [Schedonorus arundinaceus], with a few black locust trees surrounding the cave entrance. The land use type is active cattle grazing. Based on the USDA-NRCS soils report (2006), the main soil types within the area of James Cave are Slabtown silt loam, Lowell silt loam, and Wurno-Newbern-Faywood silt loam (Eagle et al., 2015). The cave system extends about 2.3 km (Eagle et al., 2015). The cave water is autogenic, with no known direct water source leading into or coming from the cave system (Eagle et al., 2015).

Soil CO_2 sensors (Vaisala GMM221, Vaisala Corporation, Finland) and soil water content and temperature sensors (CS655, Campbell Scientific, Logan, UT, United States) were installed at 20, 40, and 60 cm depths at two locations in the sinkhole, the shoulder and toeslope (Figure 1). For this study, sensors recorded on an hourly basis from 1 April 2017 through 31 March 2018 (1 year). Data were stored on a CR1000 logger (Campbell Scientific, Logan, UT). The CO_2 sensors recorded concentrations in millivolts (mV) with a range of 0 to 5566 mV. The CO_2 sensor millivolt readings were converted into parts per million by volume (ppmv) using a conversion of 1 mV = 10 ppmv. Sensor accuracy at 25°C was reported by the manufacturer as ±[2% of the sensor range + 2% of the reading], with an analog output resolution of 0.03%. All measured CO_2 concentrations were corrected to account for actual pressure and temperature using the ideal gas law. Air pressure readings came via the NOAA National Centers for Environmental Information portal from the Blacksburg Airport, which was located approximately 17 km from the study site. Temperature readings came from the adjacent soil temperature sensors.

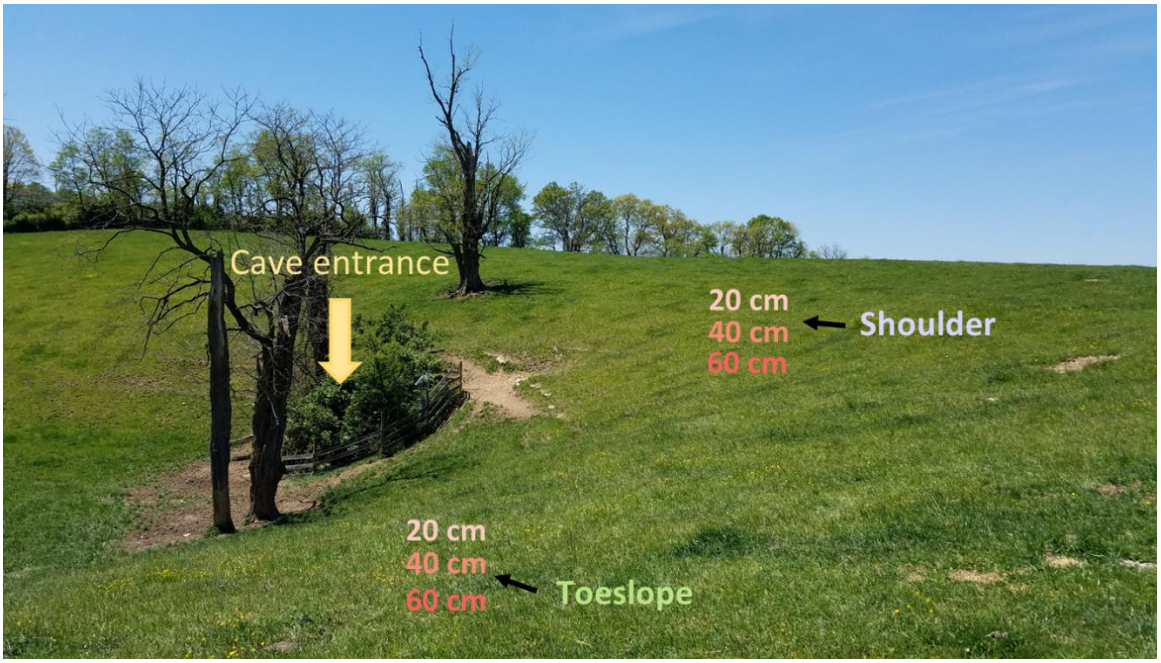

Figure 1. Conceptual figure for the locations of sensors by relative depths along the sinkhole slope relative to the cave entrance.

2.3.2 Depth of the zero-flux plane

I calculated the zero-flux plane by comparing the CO_2 concentrations at the three depths (20 cm, 40 cm, and 60 cm) for both the shoulder and toeslope sinkhole locations. The maximum CO_2 concentrations were always much greater than the assumed atmospheric CO_2 concentration of 400 ppmv. Therefore, a zero-flux plane was located in the shallow subsurface whenever the 20 cm or 40 cm sensors reported higher CO_2 concentrations than the other two depths (Figure 2a and 2b). In these instances, the zero-flux plane depth was fixed at the depth of the sensor reporting the maximum concentration. In addition, whenever the 40 cm sensor reported lower CO_2 concentrations than the 20 and 60 cm sensors, I counted that record as having a divergent zero-flux plane at 20 cm (Figure 2c). Finally, whenever the CO_2 concentration at the 60 cm depth was greater than the other two depths, I assumed that there was not a detectable zero-flux plane

in the shallow subsurface (Figure 2d). In this case, only upward CO_2 diffusion would occur. To reduce the possibility of false positives, I only considered zero-flux planes to exist for records in which the measured CO_2 concentrations differed between sensors by more than 2,500 ppmv (i.e., 5% of the sensor measurement range).

Additionally, some data gaps occurred when the local CO_2 concentrations exceeded sensor range (approximately 5.5% CO_2 concentration). If either the 20 or 40 cm sensors recorded an out-of-range value, then that depth was assumed to be the location of the zero-flux plane. If the 20 and 40 cm both reported out-of-range values, but the 60 cm sensor was in-range, then the zero-flux plane was assumed to be 40 cm deep. If the 20 and 60 cm both reported out-of-range values, then a zero-flux plane was assumed to be at 20 cm. Otherwise, I assumed that there was not a detectable near-surface zero-flux plane.

Finally, to assess seasonal differences in the zero-flux plane depth, I characterized zero-flux plane depths as being either in the warmer growing season (1 April 2017 – 30 September 2017) or in the cooler dormant season (1 October 2017 – 31 March 2018).

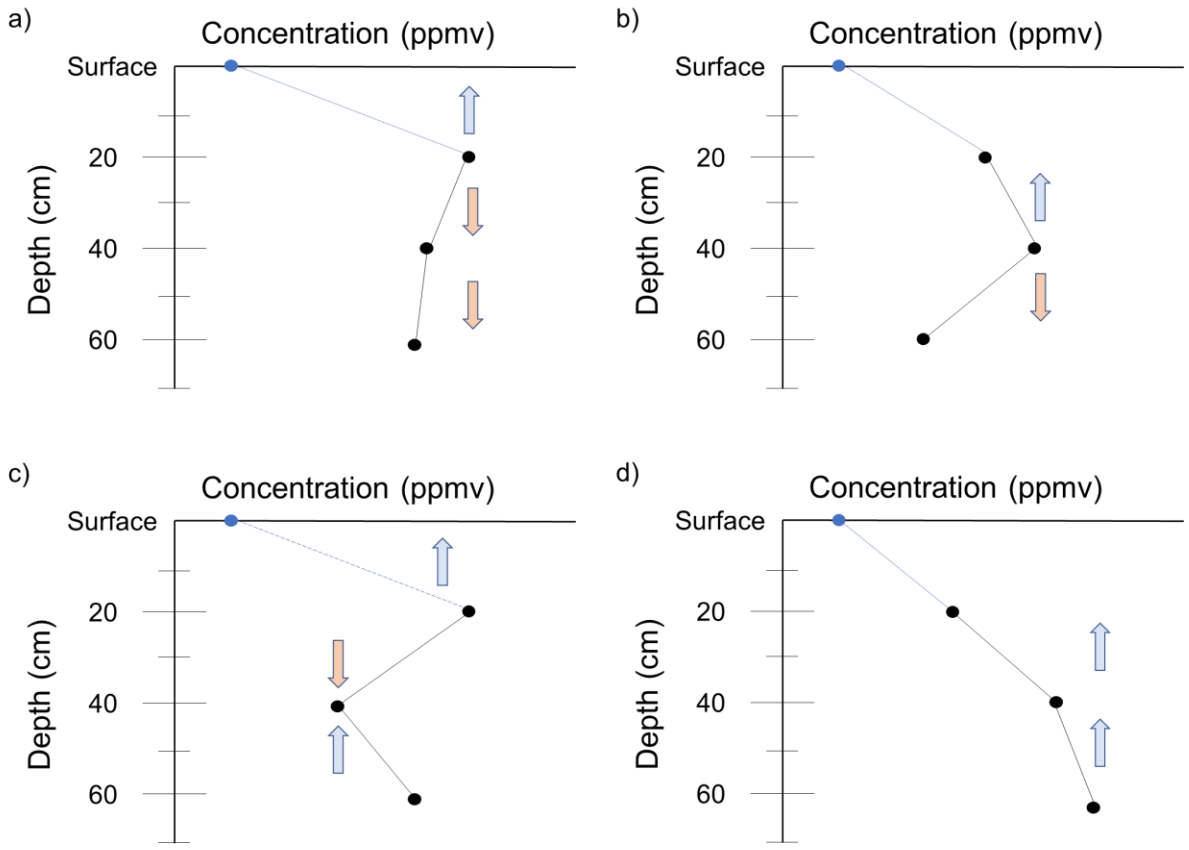

Figure 2. Example of identifying the zero-flux plane based on relative CO_2 concentrations at multiple sensors installed at discrete depths. In panel a) a divergent zero-flux plane is located near the 20 cm depth based on the maximum CO_2 concentration measured there. In panel b) a divergent zero-flux plane is located near the 40 cm depth. In panel c) a divergent plane is located near the 20 cm depth and a convergent flux plane is located near the 40 cm depth. In panel d) there is no detectable zero-flux plane, since 60 cm has the highest CO_2 concentration.

2.3.3 Concentration gradients

I calculated the concentration gradients using three sensor pairings at each location: 1) 40 cm – 20 cm, 2) 60 cm – 40 cm, and 3) 60 cm – 20 cm. The concentration gradient (G) was calculated by subtracting the measured concentration from the upper sensor from that of the lower sensor and dividing by the distance between the sensors, as shown in Equation (1):

$$G = \frac{(C_j - C_i)}{L_{j-i}} \quad (1)$$

where C_j is the CO_2 concentration from the deeper sensor [ppmv], C_i is the CO_2 concentration from the shallower sensor [ppmv], and L is the vertical distance between sensors [L].

The direction of signs in Equation (1) indicates that the positive G values correspond with the deeper sensor having a greater concentration than the shallower sensor, creating conditions for upward diffusion. Negative G values correspond to conditions for downward diffusion.

After calculating the concentration gradients, I compared the G values between the sensor pairings in two ways: 1) I calculated cumulative distributions to see if the sensor depths altered the concentration gradient distributions by the range and frequency of G, and 2) I calculated relative differences between the shallower (20 cm and 40 cm) and deeper (40 cm and 60 cm) concentration gradient pairs for a subset of readings. For the second comparison, I filtered the data and excluded any records in which the minimum or the maximum CO_2 concentrations were at 40 cm. This procedure meant that I only included records for which the zero-flux plane was at 20 cm (i.e., when the maximum CO_2 concentration was recorded at the 20 cm depth; Fig. 2a), or the maximum CO_2 concentration was at the 60 cm depth (Fig. 2d). In this way, the diffusive flux was monotonic (i.e., either upward or downward for both sensor pairings). I then calculated the relative concentration gradient (RG) using Equation (2):

$$RG = \ln\left(\frac{G_{40-20}}{G_{60-40}}\right) \quad (2)$$

where $G_{40\text{-}20}$ is the concentration gradient between the 40 and 20 cm depths and $G_{60\text{-}40}$ is the concentration gradient between the 60 and 40 cm depths.

Based on Equation (2), whenever $RG = 0$, the concentration gradients were equal in magnitude between the sensor pairs, indicating a uniform concentration gradient. When RG was positive, the concentration gradient between 40 cm and 20 cm was greater than the concentration gradient between 60 cm and 40 cm, and the opposite was true when RG was negative.

2.4 Results

2.4.1 Depth of the zero-flux plane

The depth of the zero-flux plane fluctuated through time, and was influenced by the sinkhole slope location and season (Table 1). For the annual records, the zero-flux plane was near the surface (i.e., residing at the 20 or 40 cm depths) in 12% of records for the shoulder and 27% for the toeslope. The shoulder had the same distributions between summer and winter, but the toeslope had a distinct seasonality. During the warm season, the zero-flux plane was near the surface in 16% of records, versus 37% in cool season. The majority of the time, regardless of season, zero-flux planes were not detectable in the upper 40 cm of either soil profile.

Table 1. Percentage of time the CO_2 fluxes were divergent, with a divergent zero-flux plane resided at 20 cm or 40 cm, versus was not detected (No ZFP). The data were divided by sinkhole location, shoulder and toeslope, and by season, with the warm season covering 1 April 2017 – 30 September 2017 and the cool season covering 1 October 2017 – 31 March 2018.

	20 cm	40 cm	No ZFP
Shoulder: Annual	3.1%	8.9%	88%
Shoulder: Warm Season	3.1%	8.9%	88%
Shoulder: Cool Season	3.0%	9.0%	88%
Toeslope: Annual	22%	5.0%	73%
Toeslope: Warm Season	6.2%	9.8%	84%
Toeslope: Cool Season	36.7%	0.3%	63%

2.4.2 Concentration gradients (*G*)

The *G* values calculated from the three sensor pairings displayed different distributions at the shoulder location (Figure 3). The 60 cm to 40 cm sensor pair reported negative *G* values for 20% of the readings, versus 10% for the 60 cm to 20 cm pair and 5% for the 40 cm to 20 cm pair. In contrast, the 40 cm to 20 cm sensor pair had larger (positive) *G* values than the other sensor pairs, including nearly 10% of readings in which *G* was > 50,000 ppmv CO_2 m^{-1}. The 40 cm to 20 cm and 60 cm to 20 cm sensor pairings displayed similar distributions when $G < 0$, meaning the sensor pairings recorded similar concentration gradients when the CO_2 flux was downward.

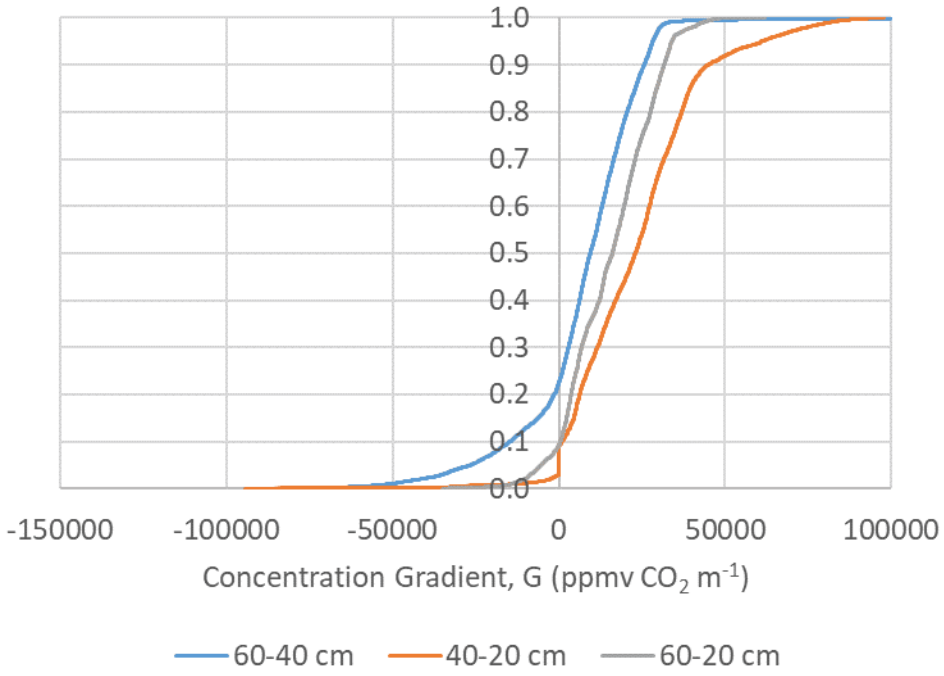

Figure 3. Distributions of the concentration gradient, G, for each of the sensor pairs: 60 cm to 40 cm, 40 cm to 20 cm, and 60 cm to 20 cm, at the shoulder location.

Unlike the concentration gradient distributions at the shoulder sinkhole location, the concentration gradient distributions at the toeslope location were almost identical between sensor pairs (Figure 4). In this part of the sinkhole, the concentration gradients between the 40 cm to 20 cm sensor pairing contained negative *G* values with the largest magnitudes. Nonetheless, the three sensor pairs had a similar proportion of negative concentrations, with $G < 0$ for 25 to 40% of records. All sensor pairings also indicated that $G > 25{,}000$ ppmv CO_2 m^{-1} for approximately 30% of the measurements.

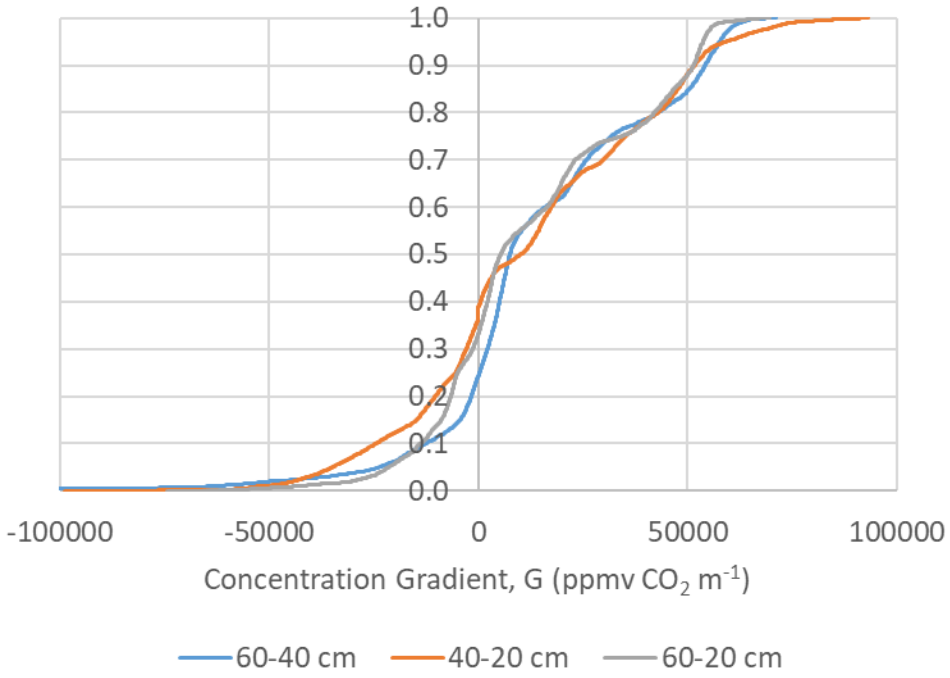

Figure 4. Distributions of concentration gradients, G, calculated at the toeslope location for the three sensor pairs: 60 cm to 40 cm, 40 cm to 20 cm, and 60 cm to 20 cm.

The distributions of *RG* values also differed depending on whether a near-surface zero-flux plane was present or not. At the shoulder location, when the zero-flux plane was located at 20 cm, the distribution of *RG* was approximately normally distributed with mean and median values close to 0 (Figure 5). When the maximum CO_2 concentration was at 60 cm deep, (i.e., no detectable zero-flux plane), the distribution of *RG* was positively skewed with a mean of 0.56 and a median of 0.41 (Figure 6).

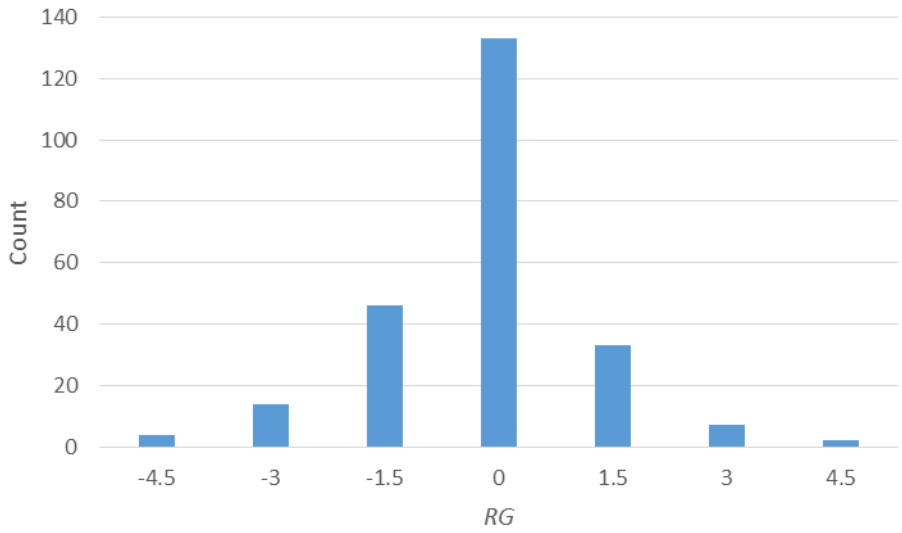

Figure 5. The distribution of the relative concentration gradient (RG) values at the shoulder location when the zero-flux plane was at 20 cm (i.e., when the maximum CO_2 concentration was 20 cm deep).

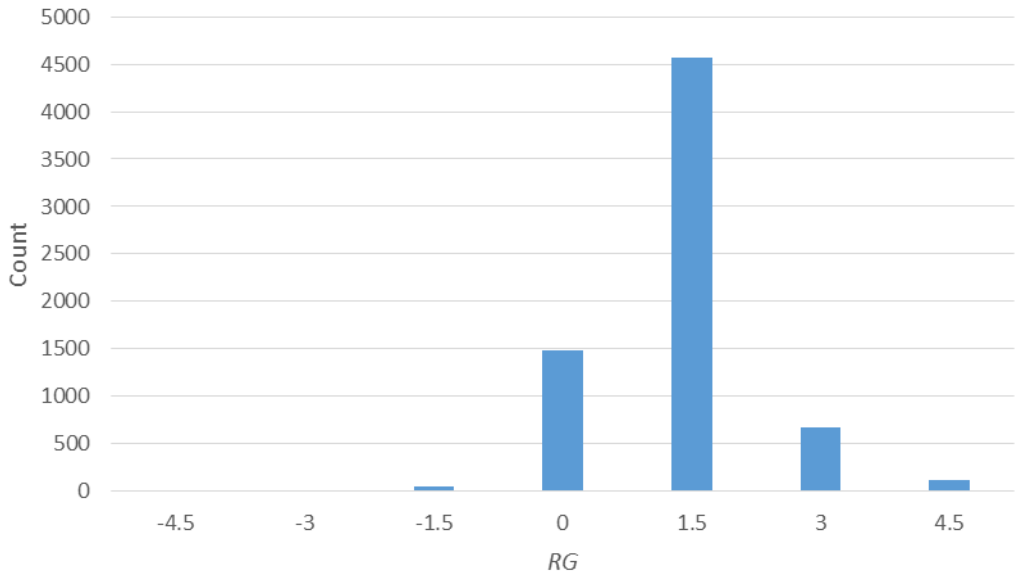

Figure 6. The distribution of the relative concentration gradient (RG) values at the shoulder location when there was not a near-surface zero-flux plane (i.e., when the maximum CO_2 concentration was 60 cm deep).

The toeslope location had opposite trends than the shoulder location. The *RG* distribution for this profile displayed a positive skew when the zero-flux plane was located at the 20 cm depth (Figure 7), with a mean of 0.56 and a median of 0.47, and displayed an approximately normal distribution when the zero-flux plane was not present (Figure 8).

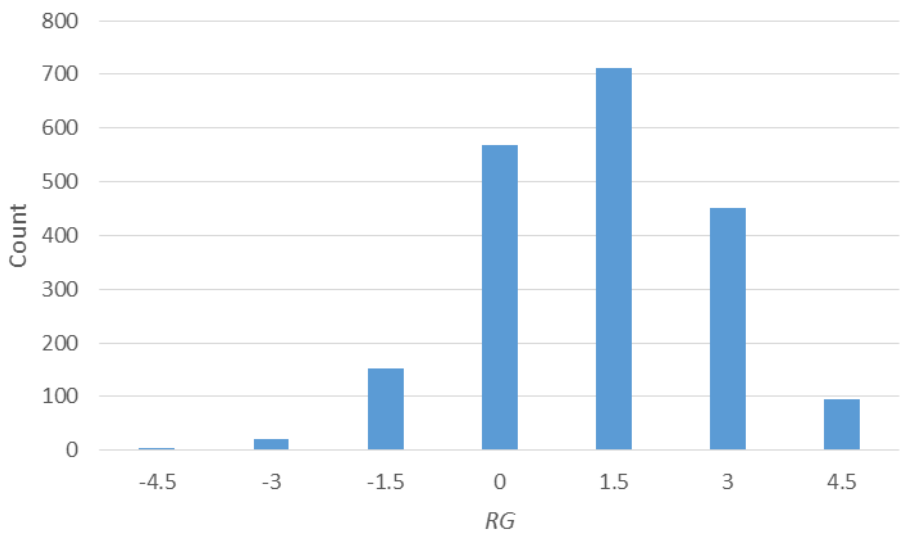

Figure 7. The distribution of the relative concentration gradient (RG) values at the toeslope location when the zero-flux plane was at 20 cm (i.e., when maximum CO_2 concentration was 20 cm deep).

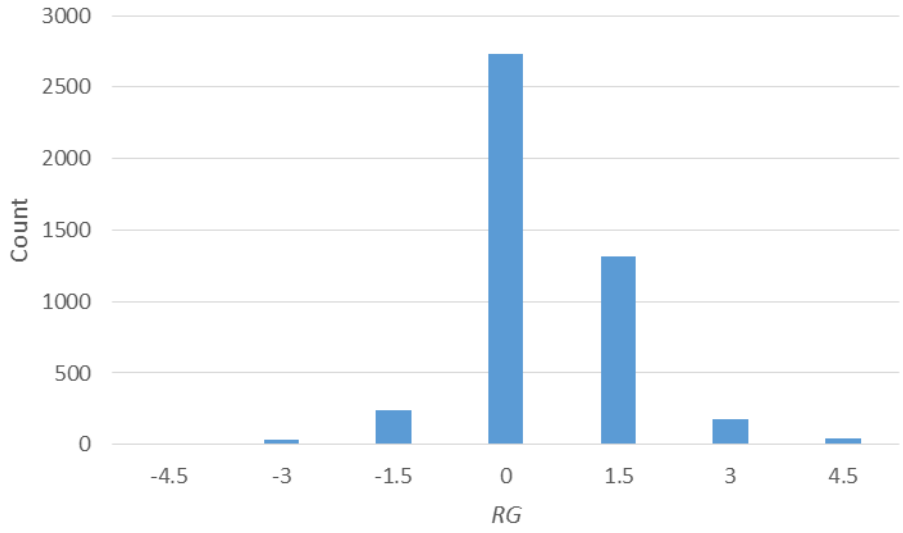

Figure 8. The distribution of the relative concentration gradient (RG) values at the toeslope location when there was not a near-surface zero-flux plane (i.e., when the maximum CO_2 concentration was 60 cm deep).

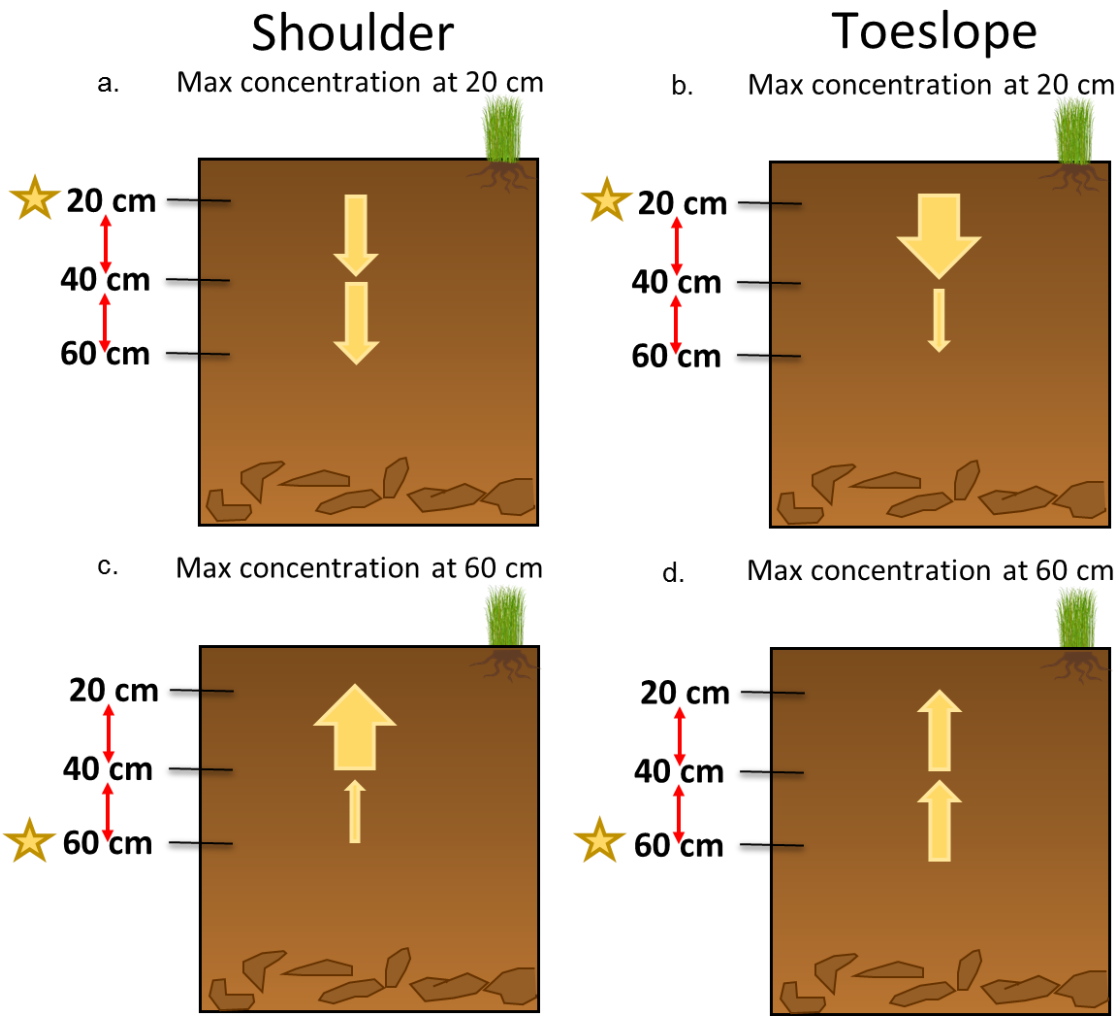

Figure 9. Conceptual figure of direction and magnitude of diffusion between the 40 cm to 20 cm and 60 cm to 40 cm sensor pairs based on RG values sorted by the depth of maximum CO_2 concentration at the 20 cm or 60 cm depths compared between the sinkhole slope positions of shoulder and toeslope. The yellow stars indicate the depth at which the maximum CO_2 concentration resided. The red arrows in between each sensor depth indicate the sensor pairs 40 to 20 cm and 60 to 40 cm. The yellow arrows indicate the direction and net magnitude of flux between the sensor pairs.

2.5 Discussion

2.5.1 Depth of the zero-flux plane

This study had three objectives: 1) quantify the frequency with which a zero-flux plane existed within the uppermost 40 cm of soil profiles at two sinkhole slope locations, 2) evaluate how the concentration gradients varied between depths, and 3) calculate relative concentration gradients to determine how often there was a uniform concentration gradient within the profiles.

2.5.2 The presence and depth of CO_2 zero-flux planes varied by season and sinkhole slope location

For the first objective, zero-flux planes were identified at the 20 and 40 cm depths throughout the study period including 12% of the time at the shoulder location and 27% of the time at the toeslope location. The two profiles also differed in the amount of time the zero-flux plane was 20 cm deep: 3.1% of the time in the shoulder versus 22% of the time in the toeslope. In such cases, the concentration gradient was much steeper between 20 cm and the soil surface (assuming an approximate atmospheric concentration of 400 ppmv) compared to the average gradient calculated from the deeper sensors. As a result, the CO_2 efflux within the system could be severely underestimated if sensors were placed at such depths that they did not detect these near-surface zero-flux planes. Further, if only a single sensor was installed, it would be impossible to detect conditions under which downward gas diffusion could occur. These results thus emphasize the importance of understanding zero-flux planes within the profile when analyzing CO_2 gas movement within karst landscapes.

The zero-flux plane depth also showed strong seasonal variance. The zero-flux plane was rarely detected during the warmer growing season (April – September), when the maximum CO_2 concentration was at 60 cm for 84% of records at the toeslope and 88% of records at the shoulder. During the cooler dormant season (October – March), the zero-flux plane was located

near the surface of the toeslope location in 37% of records. Several possible mechanisms may explain why the incidence of shallow zero-flux planes varied by season and sinkhole position. One, the lack of zero-flux planes during the summer months may be explained by high rates of microbial respiration resulting from increased soil temperature during the warm season. CO_2 production via microbial respiration increases with temperature, and can peak at temperatures around 25°C (Ali et al., 2018), which is close to the maximum soil temperatures recorded within the soil profiles in this study. It may also be possible that some CO_2 from the cave atmosphere may have diffused upward via pores and fissure networks in the subsurface when the overlying soil became sufficiently dry (Cuezva et al., 2011). At the same time, decreases in near-surface soil water content due to evapotranspiration would have increased the amount of air-filled pore space, which likely increased the soil gas diffusivity (Moldrup et al., 2000). However, large precipitation events would have increased soil water content from top-down wetting, leading to restricted diffusion pathways nearer the surface and increased CO_2 concentrations at depth (Fan & Jones, 2014; Luther-Mosebach et al., 2018; Yang et al., 2018). These occurrences could have led to the formation of temporary near-surface zero-flux planes, depending on the rates of CO_2 production at depth.

Seasonal ventilation of the cave system due to forces of natural convection could explain the frequency of the zero-flux plane residing at shallower depths ($\leq$ 40 cm) during the cool season months. Natural convection can occur in caves whenever air temperature within the cave atmosphere exceeds those of the outside atmosphere, due to buoyancy of the warm cave air (Weisbrod et al., 2009; Cuezva et al., 2011). The cave air is typically replaced by outside air that is low in CO_2. Under unsaturated conditions (i.e., when air-filled pathways exist within pores and

fissure networks), CO_2 would be able to diffuse from the soil profile into the deeper epikarst and cave layers.

Therefore, these results raise the possibility that large fracture and pore networks remain unsaturated during the cool and relatively wet seasons, particularly at the toeslope location. Previous work within James Cave used cave drip patterns to identify three different periods of hydrological recharge in the system (Eagle et al., 2015). In particular, a dry season was identified that typically started in September and then extended to December or even February or March in some years. Indeed, a subsequent analysis showed that the dry period during 2017-2018 continued until the end of January 2018 (Groce-Wright, 2021). These results provide additional evidence that large fracture and pore networks likely remained unsaturated throughout much of the cool season evaluated here (October 2017 – March 2018).

2.5.3 Concentration gradients often differed between depths within these soil profiles

When the three sensor pairings were compared, some similarities and differences emerged. For example, at the shoulder location, the deeper sensor pair (60 to 40 cm) had a higher proportion of negative *G* values compared to the other pairs, and the 40 to 20 cm sensor pair had the highest proportion of large *G* values. These results reflect conditions in which the zero-flux plane is located at depth ≤ 40 cm and the fluxes are diverging. For the toeslope location, the three sensor pairings displayed relatively similar distributions. However, the 40 to 20 cm sensor pairing had the highest proportion of negative *G* values compared to the other sensor pairings. These results most likely are explained by near-surface zero-flux planes that formed when the 40 cm CO_2 concentration was less than the 20 and 60 cm concentrations. As shown in Figure 2c, this condition could cause large downward gradients between 20 and 40 cm, thus translating to a higher proportion of negative values for that pairing.

As the sensors within each profile had even vertical spacing (i.e., 20 cm), the 60 to 20 cm sensor pairing always provided an average of the *G* values for the 40 to 20 cm and 60 to 40 cm sensor pairs for each individual record. Despite this fact, the 60 to 20 cm pairing only displayed an intermediate distribution between the other sensor pairings in the sinkhole shoulder. For the toeslope location, by contrast, the 60 to 20 cm sensor pairing reflected a very similar distribution as the 60 to 40 cm pairing while being more distinct from the 40 to 20 cm pairing. This result may again reflect the influence of times in which the 40 cm sensor had lower CO_2 concentrations than the other two sensors.

2.5.4 The assumption of a uniform CO_2 concentration gradient throughout the profile was often invalid

To fulfill Objective 3, relative concentration gradients (*RG*) were compared between the uppermost soil layer (40 to 20 cm) and the deeper soil layer (60 to 40 cm). This analysis was limited to data with monotonic concentration gradients (i.e., maximum CO_2 concentrations at either 20 or 60 cm depth).

When the data were grouped according to the depth of maximum CO_2 concentration, the importance of the sinkhole position was illuminated. When there was no zero-flux plane in the soil profile (i.e., maximum concentration at 60 cm), the *RG* values were very large for the shoulder location, indicating that the 40 to 20 cm sensor pairing was net greater than the 60 to 40 cm sensor pairing. This could be due to an increase in CO_2 production rates at an intermediate depth (between 40 and 60 cm) coupled with more rapid diffusion from the soil surface due to dry conditions leading to an increase in air-filled porosity near the surface. Gas diffusion is dependent on air-filled porosity (Moldrup et al., 2004; Werner et al., 2004) and gas diffusion rates typically increase with air-filled porosity (Fan & Jones, 2014). So, near-surface drying

conditions during the warmer months could be a factor causing the non-uniformity in the concentration gradient throughout the soil profiles. However, for the toeslope location, the *RG* values tended to be > 0 when the zero-flux plane was located at the 20 cm depth (the 40 to 20 cm sensor pairing was net greater than the 60 to 40 cm pairing), indicating that a plausible explanation could be CO_2 consumption at depth due to CO_2 consumption during the formation of carbonic acid, H_2CO_3 (Cao et al., 2020; Serrano-Ortiz et al., 2010; Zhao et al., 2021).

2.5.5 Conclusions and Implications of the Study

This study offered new insight to the importance of sensor depths when calculating CO_2 concentration gradients within karst soils. This study can inform future sensor installation depths, as most studies have only performed multiple sensor installations at relatively shallow depths: Tang et al. (2003) installed three sensors at 2, 8, and 16 cm depths, Crowther (1984) installed sensors at 15, 30, and 50 cm, Fan & Jones (2014) installed sensors at 5, 10, and 15 cm depths, Jassal et al. (2005) installed sensors at 5, 10, 20, and 50 cm depths, Pingintha et al. (2010) installed sensors at 2 and 12 cm depths, Xiao et al. (2015) installed sensors at several depths ranging from 0 to 20 cm, Yang et al. (2018) installed sensors at 5 and 15 cm depths within soil columns, among many other studies. Such studies with relatively shallow multiple sensor installation depths are suitable for measuring CO_2 efflux from the soil surface, but deeper installation may be necessary to identify zero-flux planes and understand downward diffusion.

In this study the deepest sensors were installed at 60 cm, which is relatively deep compared to many other studies. However, this depth still may not have been adequate to identify all zero-flux plane conditions. Specifically, for the records in which the maximum concentration was located at the 60 cm depth, it was unknown if a zero-flux plane existed at that depth or not due to the unknown CO_2 dynamics below the 60 cm depth. Future studies could incorporate CO_2

concentration data from depths surpassing 60 cm in depth in order to investigate the possibility of zero-flux planes existing at depths deeper than the 60 cm depth. Such studies could include measured or presumed cave CO_2 concentrations to investigate zero-flux planes at depth.

At the same time, the study results compiled here show that near-surface CO_2 dynamics are often decoupled with CO_2 dynamics at depth. An example of this decoupling comes from the relative concentration gradients (*RG*), which varied from 0 depending on the presence of a zero-flux plane at 20 cm or no zero-flux plane in the soil profile for both sinkhole slope locations. At the shoulder location, *RG* values were larger when the soil profile did not have a zero-flux plane, whereas at the toeslope location the *RG* values were larger when the zero-flux plane was located at the 20 cm depth. In both cases, the larger *RG* values indicated that the 40 to 20 cm sensor pair was identifying larger gradients than the 60 to 40 cm sensor pair. These results provide examples of decoupled CO_2 dynamics between the near-surface (i.e., the 40 to 20 cm sensor pairing) and at depth (i.e., the 60 to 40 cm sensor pairing) because of the non-uniform concentration gradient throughout the profile. One possible explanation for this decoupling is downward transport of CO_2 dissolved in water as carbonic acid, H_2CO_3, which could decrease CO_2 concentrations in the lower part of the soil profile (Serrano-Ortiz et al., 2010).

Finally, the studied sinkhole was located just above a karst cave system. The primary method of CO_2 transfer from the near-surface to the cave atmosphere is understood to be via advection through the consumption of atmospheric and soil CO_2 into solution percolating into the cave system and outgassing out of solution into the cave atmosphere (Mattey et al., 2016) and this process may be coupled to diffusion. Thus, from this study, it seems that CO_2 may also diffuse downward into the cave system. Future studies could investigate the movement of CO_2 both upwards and downwards from the vadose zone using carbon isotopic discrimination methods

(Breecker et al., 2012) to track the timing and sources of carbon, as well as measuring porous connectivity within and below the vadose zone to track the restriction of gas diffusivity exiting the vadose zone. These studies will aid in the advancement of knowledge for CO_2 dynamics within karst systems.

3. Landscape and seasonal influences on CO_2 fluxes within a karst sinkhole

3.1 Abstract

Processes affecting subsurface soil carbon dioxide (CO_2) diffusion remain poorly understood particularly in karst landscapes, which are characterized by easily weathered rock and the presence of subsurface fracture and cave networks. In order to better understand controls on soil CO_2 diffusion in karst, I instrumented three soil profiles with solid-state CO_2 sensors and soil water content/temperature sensors at three depths (20, 40, and 60 cm) along a sinkhole slope. I then calculated CO_2 flux using Fick's Law and measured porosity, volumetric water content, and soil temperature values. All profiles had strong seasonal differences in CO_2 fluxes, with relatively large upward fluxes during the warm season months. These upward CO_2 fluxes were smallest in the shoulder and backslope of the sinkhole (peaking at around 1.0 μmol CO_2 m^{-2} s^{-1}), and largest at the toeslope (peaking at around 2.4 μmol CO_2 m^{-2} s^{-1}). During the cool-season months, upward CO_2 fluxes were smaller and were often counteracted by downward fluxes of similar magnitude. These downward fluxes may be attributable to natural ventilation processes occurring within the underlying cave system, which likely decreased CO_2 gas concentrations at depth. Cumulative annual CO_2 efflux at the toeslope profile equaled 16.0 mol CO_2 m^{-2}, which was 3-4 times larger than efflux from the other two profiles. However, these annual efflux estimates were sensitive to the assumed soil porosity values, with up to an order of magnitude difference when the porosity value was assumed to be relatively small (i.e., 0.40 cm^3 cm^{-3}) as opposed to relatively large (i.e., 0.56 cm^3 cm^{-3}). These findings highlight that karst soils have high spatial and temporal variability in their CO_2 fluxes, and also suggest that the presence of subsurface fractures and caves may influence soil CO_2 dynamics.

3.2 Introduction

Exchange of carbon dioxide (CO_2) from the land surface to the atmosphere is an important term in the global carbon cycle; however, in many systems the controls and magnitudes of CO_2 emissions from the soil surface are not well understood. These dynamics are particularly important in karst regions, which are characterized by relatively soluble carbonate rock, usually dolomite or limestone rock, and occupy as much as 15% of the global land surface (Fang et al., 2012; Ford & Williams, 2007). Over timescales of thousands to hundreds of thousands of years, karst regions absorb CO_2 when it becomes converted into HCO_3 during chemical weathering of rock (Chen, 2019; Xie et al., 2021; Zhao et al., 2021; Zhao et al., 2019). At the same time, much of the CO_2 involved in the karst weathering process comes from overlying soils or the atmosphere (Chen, 2019; Xie et al., 2021; Zhao et al., 2021; Zhao et al., 2019) Thus, understanding the magnitudes and directions of CO_2 fluxes in karst soils is necessary to perform accurate regional and global carbon budgeting.

Subsurface CO_2 transport occurs via two processes, diffusion and advection (i.e., mass flow). Advection is the mass flow of CO_2 in which the gas is transported via flowing wind or water, typically at a relatively constant concentration. Diffusion occurs due to concentration gradients driving CO_2 to move from areas of high to low concentration. In most soils, diffusion is the more important process, due to limited bulk air or water movement (Hillel, 2003; Jin & Jury, 1996; Schjønning et al., 2013; Pumpanen et al., 2003; Laemmel et al., 2017). The rate of gas diffusion depends on two factors: 1) a diffusion coefficient, D_s, and 2) a concentration gradient, ($\Delta C/\Delta x$). The diffusion coefficient is a measure of the rate of movement of a gas under constant temperature and pressure conditions through a uniform medium. In soils, the diffusion coefficient is affected by several factors, with the volume of air-filled pore space representing a

particularly important term (Lafond et al., 2011; Jin & Jury, 1996). While some field methods exist to quantify D_s (Allaire et al., 2008; Shcherbak & Philip Robertson, 2014), usually that parameter is quantified with intact or repacked soil cores in a laboratory setting (Iiyama & Hasegawa, 2005; Kristensen et al., 2010), as it is otherwise difficult to control environmental conditions such as water content, temperature, and pressure in the field.

The concentration gradient can be quantified by measuring partial pressures, or equivalent molar concentrations, at multiple depths (Tang et al., 2003). Previous studies have shown that CO_2 concentrations within karst caves can be up to two orders of magnitude greater than atmospheric concentrations (Trinh et al., 2018), and that soil CO_2 concentration tends to increase with depth (Benavente et al., 2010; Tang et al., 2003; Chen, 2019). However, other studies have identified conditions under which soil CO_2 concentrations near the surface are greater than those at depth (Benavente et al., 2010; Chen, 2019). In such instances, a zero-flux CO_2 plane will exist in the subsurface, and gas will diffuse from that location both upward toward the soil surface and downward toward the deeper karstic layers. This formation and frequency of zero-flux planes is discussed in detail in Chapter 2; however, the influence of near-surface zero-flux planes on carbon movement via gas diffusion remains poorly understood.

To address this knowledge gap, I investigated trends of CO_2 fluxes in a sinkhole that overlies a karst cave system. Working at three sinkhole slope locations – shoulder, backslope, and toeslope – I collected hourly CO_2 concentrations at three depths (20, 40, and 60 cm) and quantified CO_2 fluxes between February 2017 and September 2019. My first study objective was to quantify spatial differences in CO_2 fluxes between the three sinkhole positions. I hypothesized that the shoulder would have the largest upward CO_2 fluxes (i.e., CO_2 diffusing toward the soil surface) and smallest downward fluxes (i.e., CO_2 diffusing away from the soil surface), as this location

had the largest vertical distance from the underlying cave system. I also hypothesized that the toeslope would have larger downward CO_2 fluxes and relatively smaller upward fluxes due to CO_2 movement toward the cave. My second study objective was to examine seasonal trends in CO_2 fluxes. Here I hypothesized that CO_2 fluxes would be smaller and net downward (i.e., downward fluxes exceeding upward ones) during cooler months of the year, when near-surface soils were relatively wet, and therefore had low gas diffusion rates, and also because CO_2 may escape through the underlying cave system due to convective venting that often occurs in the wintertime (Krajnc et al., 2017; Mattey et al., 2016). Conversely, I hypothesized that CO_2 fluxes will be larger and net upward during warmer months of the year, since autotrophic and heterotrophic respiration typically increase with temperature and gas diffusion rates typically increase with lower soil water contents (Ali et al., 2018; Fang & Moncrieff, 2005).

3.3 Methods

3.3.1 Site description

The site is located at James Cave in southwest Virginia, United States. James Cave is defined as a doline karst cave system with large amounts of limestone and dolomite rock (Eagle et al., 2015). Based on the USDA-NRCS soil report (2006), the soils surrounding James Cave are classified as Slabtown silt loam, Lowell silt loam, and Wurno-Newbern-Faywood silt loam (Eagle et al., 2015).

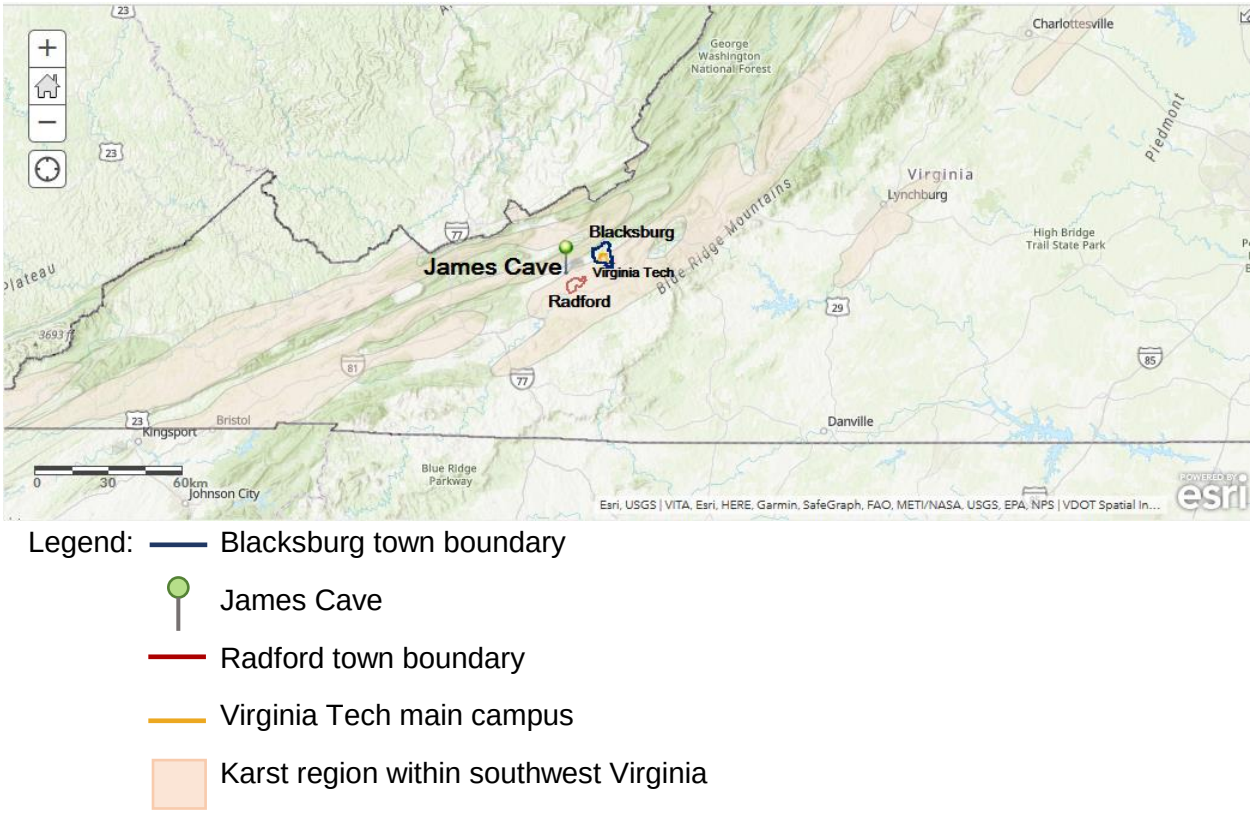

Figure 1. Location of the study site at James Cave in southwest Virginia, United States. The karst layer was downloaded from ArcGIS on April 8, 2021 (https://services1.arcgis.com/TQSFiGYN0xveoERF/arcgis/rest/services/karst_and_virginia/FeatureServer).

In 2015, sensors were installed in the sinkhole that surrounds the entrance to James Cave, with vertical profiles instrumented at the shoulder, backslope, and toeslope of the sinkhole slope. Each

profile contained three CO_2 sensors (Vaisala GMM221, 5% maximum concentration, Vaisala Corporation, Finland) and three soil water content and temperature sensors (CS655, Campbell Scientific, Logan, UT, United States) located at 20, 40, and 60 cm below the surface. The data were measured every hour using a CR1000 logger (Campbell Scientific, Logan, UT).

All installed sensors functioned from 7 February 2017 through 18 April 2018, when the 40 cm CO_2 sensor at the shoulder location failed. The 40 cm CO_2 sensor failed at the toeslope location on 30 April 2018, followed by the 40 cm deep CO_2 sensor at the backslope, which failed on 11 June 2018. The 20 cm sensor at the backslope failed on 8 July 2018, and the 60 cm deep sensor at the shoulder location failed on 24 September 2018. The 60 cm CO_2 sensor in the backslope profile failed on 30 June 2019 and the shallowest (20 cm) CO_2 sensors failed on 22 June 2019 at the shoulder and on 19 September 2019 at the toeslope. Finally, the 60 cm sensor at the toeslope failed on 30 September 2019. Therefore, all three profiles had a common 1.5-year period in which the deepest and shallowest sensors were operated, and the toeslope had an additional year over which both sensors functioned. The barometric pressure and hourly precipitation data were downloaded through NOAA's National Centers for Environmental Information (NCEI) from Integrated Surface Database for the Blacksburg Airport station, which was located approximately 17 km from the study site. Temperature readings came from the adjacent soil temperature sensors.

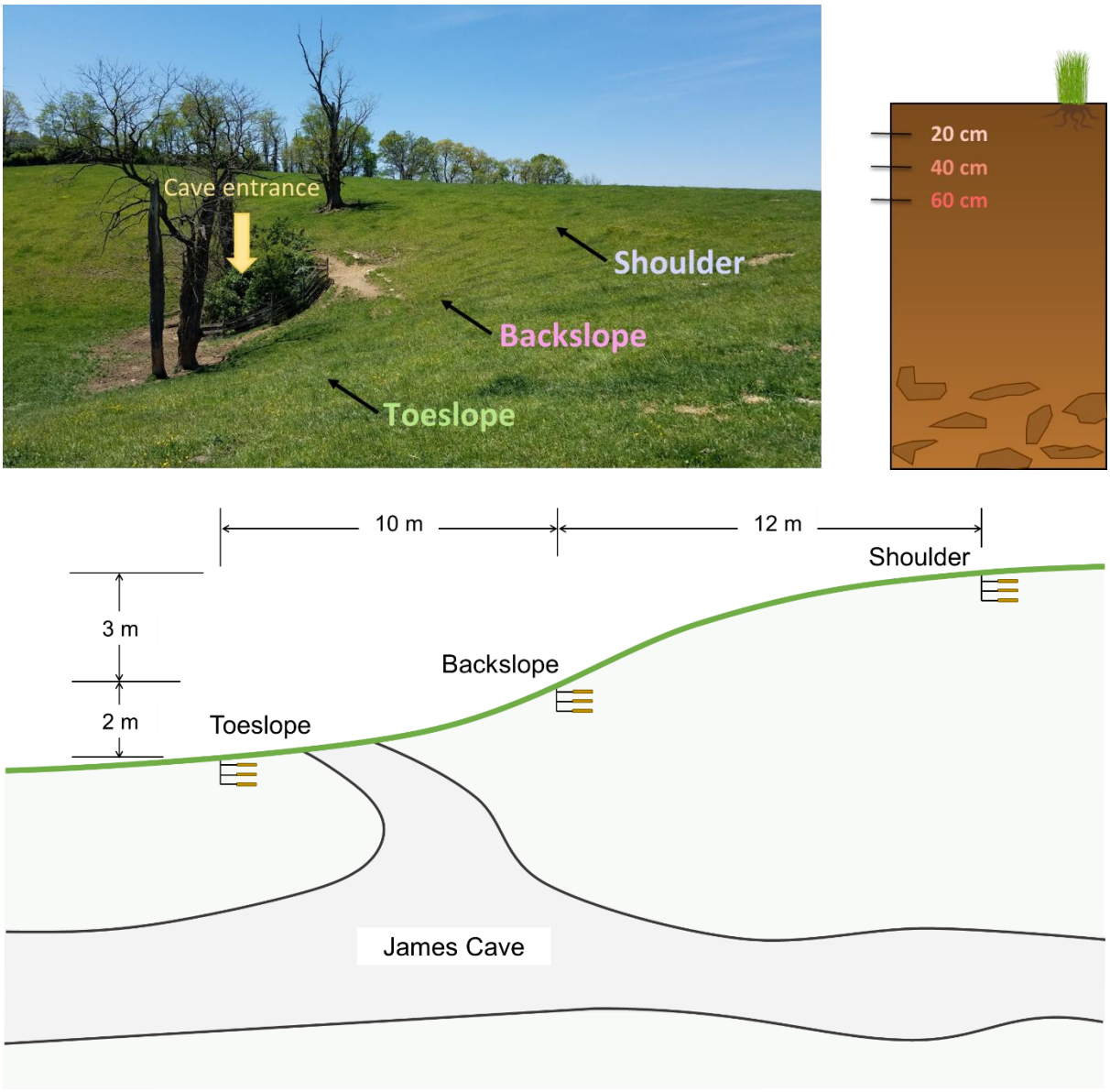

Figure 2. (Left) Study site near the entrance of James Cave, Virginia, United States. The cave entrance and three instrumented profiles are indicated by text. (Right) Schematic of the soil profiles showing depths of CO_2 and soil water content/temperature sensors. (Bottom) Cross-section of study site including horizontal and vertical dimensions between the sinkhole slope locations and associated sensor depths relative to the sinkhole slope and James Cave entrance.

Soil Characterization

Volumetric soil cores were collected from the site in order to determine hydraulic properties. The cores were collected from the depths of 15, 20, 35, and 40 cm for the shoulder location and from the 15, 20, and 40 cm depths for the backslope and toeslope locations. The cores were first saturated with 0.01 M $CaCl_2$ solution and were then analyzed for saturated hydraulic conductivity (K_{sat}) using a falling head permeameter (K_{sat} Device, METER Group, Pullman, WA, U.S.), with 3-4 repeated measurements conducted per core to obtain a mean K_{sat} value. The cores were then measured for water retention using a positive pressure system (SoilMoisture, Inc., Santa Barbara, CA, U.S.). Soil water content was determined at pressure heads of 0 cm (saturation), -340 cm (field capacity), -1,020 cm, and -3,060 cm. The soil water content at the pressure head of 0 cm was considered to be equivalent to porosity. Soil water retention curve parameters (θ_r, θ_s, α, n) were then estimated using a least-squares regression between the measured data and the van Genuchten (1980) hydraulic model. The volumetric soil core samples were also analyzed for bulk density by dividing the dry soil mass by total volume. Soil dry weight was calculated by subtracting the ring mass, cheese cloth mass, and rubber band mass from the dry weight of the soil to get soil weight.

3.3.2 CO_2 Flux Calculations

The measured CO_2 concentrations were corrected for temperature and pressure based on the ideal gas law (Vaisala, 2017):

$$C_{corrected} = C_{measured}\left(\frac{P_{std}}{RT_{std}}\right) \quad (1)$$

where $C_{corrected}$ is the CO_2 concentration corrected for temperature and pressure (in μmol m^{-3}), $C_{measured}$ is the measured CO_2 concentration (in μmol CO_2 mol^{-1} air), P_{std} is the standard barometric pressure used in the instrument calibration (101.3 kPa), T is the standard temperature

used in the instrument calibration (298 K), and R is the ideal gas law constant (8.31 x 10^{-3} kPa m^3 mol^{-1} K^{-1}).

After adjusting the measured concentrations for temperature and pressure, I calculated CO_2 fluxes (in μmol CO_2 m^{-2} s^{-1}) utilizing Fick's Law:

$$Flux = -D_s \frac{\Delta C}{\Delta x} \quad (2).$$

where ΔC is change in concentration (μmol m^{-3}) and Δx is the change in distance (m), and D_s is the diffusion coefficient (m^2 s^{-1}). D_s was calculated following Tang et al. (2003):

$$D_s = D_0 \left(\frac{\varepsilon^{10/3}}{\phi^2}\right) \quad (3)$$

$$\varepsilon = \phi - \theta \quad (4)$$

$$D_0 = D_{a0} \left(\frac{T}{293.15}\right)^{1.75} \left(\frac{P}{101.3}\right) \quad (5)$$

where ε is the air-filled porosity (cm^3 cm^{-3}), ϕ is the soil porosity (cm^3 cm^{-3}), θ is the soil volumetric water content (cm^3 cm^{-3}), T is temperature (°K), P is pressure (kPa), and D_{a0} is the gas diffusivity in pure air under standard temperature (293.15 °K) and pressure (101.3 kPa) conditions. When calculating Equations (3) and (4), I used mean θ and T values measured for each soil profile (i.e., the mean values between the 20 cm and 60 cm sensors). Porosity, ϕ, was determined based on the mean volumetric saturated water content (θ_s) from the soil cores collected in each profile. I assumed D_{a0} was equal to 14.7 mm^2 s^{-1} based on previous work by Tang et al. (2003).

The depths used to calculate concentration gradients ($\Delta C/\Delta x$) varied depending on whether a near-surface zero-flux plane existed or not. As detailed in Chapter 2, I assumed there was no

detectable near-surface zero-flux plane any time that the 60 cm sensor had the highest concentration or that sensor reported an out of range concentration (>5.5% CO_2). To avoid false positives associated with instrument error, I also assumed that there was no near-surface zero-flux plane whenever the 20 and 40 cm sensors recorded concentrations that were within 2,500 ppmv of the 60 cm sensor (representing 5% of the sensor range). For all of these instances, I calculated a single $\Delta C/\Delta x$ value as the average of 1) the difference in measured CO_2 concentrations at 60 and 20 cm depths divided by the distance between these points (i.e., 40 cm), and 2) the difference between the measured CO_2 concentration at 20 cm depth and an assumed atmospheric concentration of 400 ppmv at the surface, divided by the 20 cm distance between those points.

A near-surface zero-flux plane was identified at 20 cm whenever that sensor reported CO_2 concentrations more than 2,500 ppmv larger than those of the 40 and 60 cm sensors, and a zero-flux plane was assumed to be at 40 cm whenever the CO_2 concentration there exceeded the 60 cm concentration by at least 2,500 ppmv. The 40 cm deep sensors were the first to fail in all three profiles, so once those sensors stopped recording I considered a near-surface zero-flux plane to exist whenever the 20 cm deep concentration exceeded the 60 cm deep concentration by at least 2,500 ppmv. I then calculated two concentration gradients for all records associated with a shallow zero-flux CO_2 plane. The upward concentration gradient was calculated using differences in CO_2 concentrations between the sensor associated with the zero-flux plane and the atmosphere (once again assumed to be 400 ppmv), divided by the depth of the zero-flux plane. The downward concentration gradient was calculated using the difference between the maximum measured CO_2 concentration and the concentration measured at 60 cm, divided by the distance

between the sensors. Once either of the 20 or 60 cm sensors failed, it was no longer possible to estimate a downward concentration gradient or flux.

Finally, I quantified seasonal and annual CO_2 fluxes from each profile, with the upward (i.e., efflux from the soil surface) and downward fluxes calculated separately for each profile. Annual fluxes were calculated by summing hourly fluxes between 1 April 2017 and 31 March 2018. For the seasonal fluxes, I divided the data into a warm season from 1 April 2017 to 30 September 2017, and a cool season, from 1 October 2017 to 31 March 2018. I used linear interpolation to fill gaps in the hourly flux records, using the flux values that were calculated immediately before and after the missing records. This approach gave similar values as using only records with measured fluxes (data not shown), indicating that the linear interpolation process did not appear to overly influence the results.

3.3.3 Sensitivity analysis

I performed a brief sensitivity analysis to test how the porosity (ϕ) term in Equations (3) and (4) affected D_s and CO_2 flux values. First, I calculated D_s through time for each profile using five assumed porosities: ϕ = 0.40, 0.44, 0.48, 0.52, and 0.56 $cm^3\ cm^{-3}$. These porosities reflected the range of values measured in the soil samples used for soil characterization. I next used Equations (2) – (5) to determine CO_2 fluxes for each profile, and then summed the cumulative CO_2 emissions for the period between 1 April 2017 and 31 March 2018.

3.4 Results

Based on the soil sample characterization, bulk densities ranged from 1.07-1.30 g cm^{-3} (Table 1). The porosity values ranged between 0.40-0.55 $cm^3\ cm^{-3}$, with a mean of 0.44 $cm^3\ cm^{-3}$.

Table 1. James Cave soil characterization based on the soil samples collected at varying depths at the three sinkhole slope locations. K_{sat} values indicate mean ± standard deviation.

Sample	Location	Depth (cm)	K_{sat} (cm/d)	Bulk density (g/cm^3)	Porosity (cm^3/cm^3)
1	Shoulder	15	2197 ± 756	1.17	0.44
2	Shoulder	20	3822 ± 786	1.22	0.44
3	Shoulder	35	88 ± 96	1.30	0.40
4	Shoulder	40	284 ± 67	1.03	0.47
5	Backslope	15	4245 ± 1322	1.20	0.40
6	Backslope	20	1740 ± 137	1.20	0.41
7	Backslope	40	700 ± 553	1.04	0.49
8	Toeslope	15	2480 ± 62	1.10	0.43
9	Toeslope	20	1503 ± 15	1.07	0.55
10	Toeslope	40	1176 ± 303	1.13	0.41

The water retention curves were similar between most soil cores (Figure 3). Saturated water content, θ_s, varied between 0.41 and 0.55 $cm^3\ cm^{-3}$ for the toeslope location, between 0.41 and 0.49 $cm^3\ cm^{-3}$ for the backslope location, and between 0.40 and 0.47 $cm^3\ cm^{-3}$ for the shoulder location. Based on these results, when calculating D_s values (Equation 3), I assumed mean ϕ values of 0.48 $cm^3\ cm^{-3}$ for the toeslope profile, 0.45 $cm^3\ cm^{-3}$ for the backslope profile, and 0.44 $cm^3\ cm^{-3}$ for the shoulder.

The three sinkhole slope positions also had similar ranges for other measured water contents. For example, at field capacity (i.e., pressure head = -340 cm), volumetric water content values were between 0.32 and 0.41 $cm^3\ cm^{-3}$ for the toeslope location, between 0.33 and 0.39 $cm^3\ cm^{-3}$ for the backslope location, and between 0.33 and 0.38 $cm^3\ cm^{-3}$ for the shoulder location. The residual water content, θ_r, values ranged between 0.10 and 0.22 $cm^3\ cm^{-3}$.

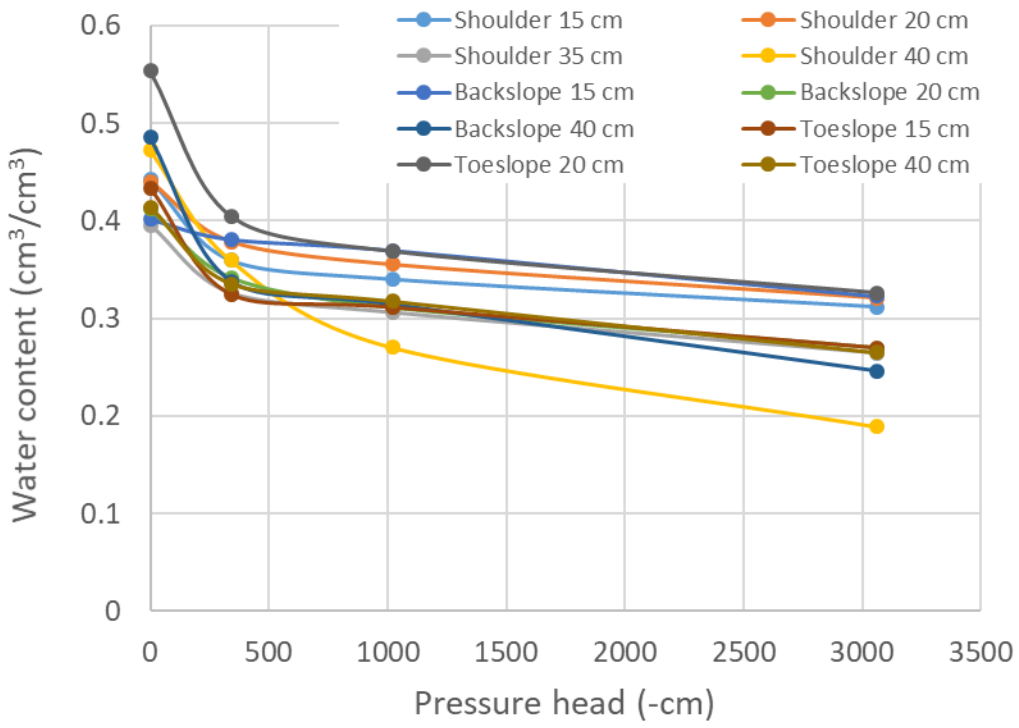

Figure 3. Soil water retention curves for samples collected within the three soil profiles (shoulder, backslope, and toeslope).

3.4.1 Volumetric water content

Volumetric water contents were lower in the summer and fall months with a range of 0.10 to 0.35 cm^3 cm^{-3} (Figure 4). Contrarily, the greatest precipitation events were in the summer and fall months with a range of 1.0-2.5 cm recorded hourly (Figure 4). During the cool season (the months of October through March), the volumetric water contents were higher, fluctuating between 0.30 and 0.45 cm^3 cm^{-3}. The shoulder and toeslope locations experienced the greatest seasonal variation in volumetric water contents, while the backslope had smaller magnitude changes.

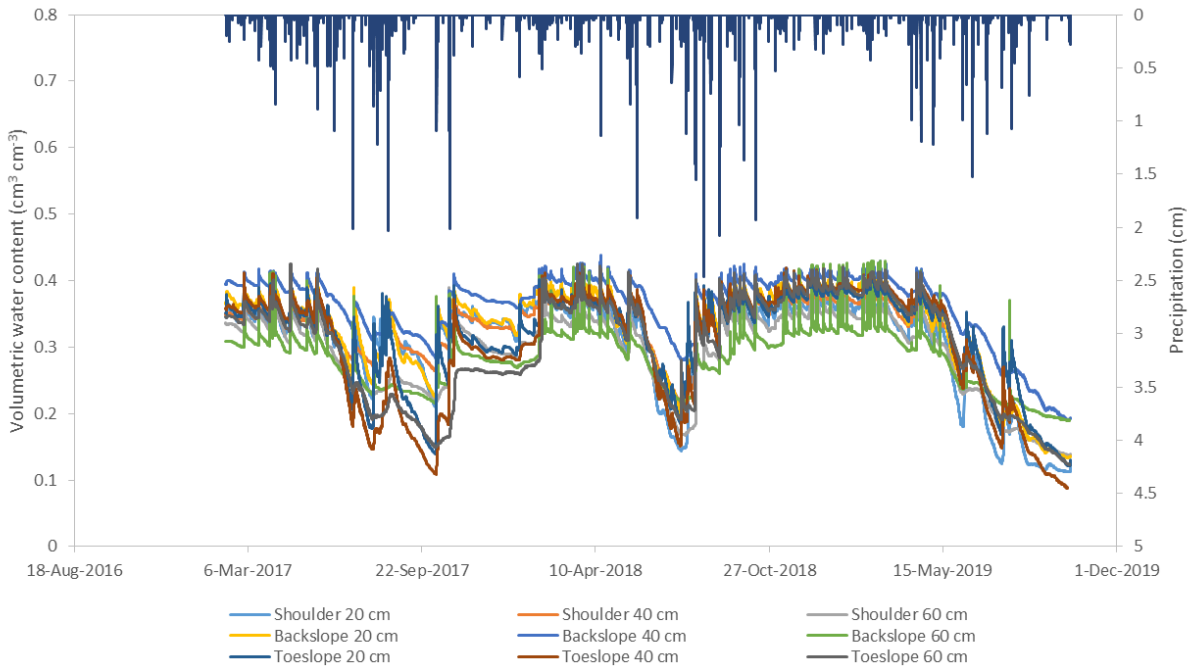

Figure 4. Hourly precipitation data (cm) and volumetric water content (cm^3 cm^{-3}) from February 2017 through September 2019 for three sinkhole slope positions - shoulder, backslope, and toeslope - at 20, 40, and 60 cm depths.

3.4.2 Soil temperature

The soil temperature fluctuated seasonally (Figure 5), varying between 15 °C and 26 °C for the warmest months (June-September) and between 1 °C and 13 °C in the coolest months (December-March). During the months of March through May and September through November, soil temperatures transitioned between the extremes seen in the cooler and warmer months.

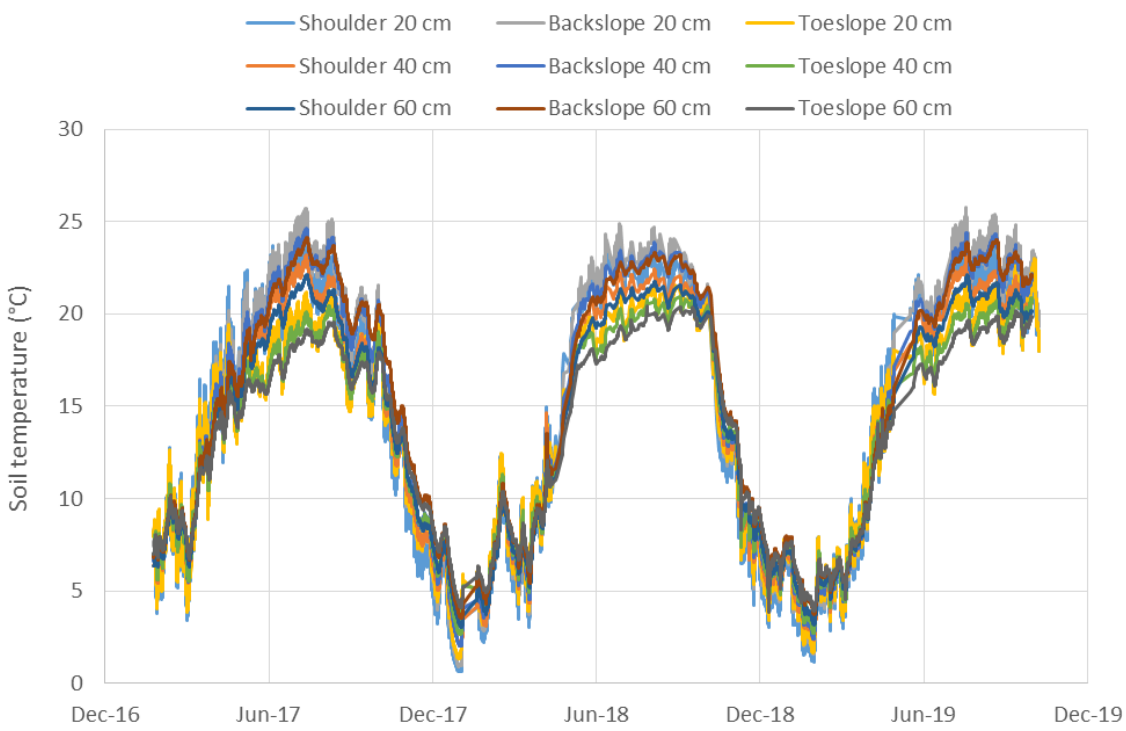

Figure 5. Soil temperatures (°C) at 20, 40, and 60 cm depths for the sinkhole shoulder, backslope, and toeslope profiles from February 2017 through September 2019.

3.4.3 Gas Diffusivity

The calculated D_s term had a seasonal pattern in all three profiles (Figure 6). D_s values increased during each warm season, peaking between July and September. The values then decreased, becoming 1 to 2 orders of magnitude lower by the end of each cool season. In the first year of the study, D_s was typically highest in the toeslope location and lowest in the shoulder location. In the second and third year of the study, the backslope often had the lowest D_s values, and the shoulder and toeslope profiles had similar magnitudes. Depending on the year, the maximum D_s values ranged between 0.5 and 1.5 $mm^2\ s^{-1}$, whereas the minimum D_s values approached 0 $mm^2\ s^{-1}$.

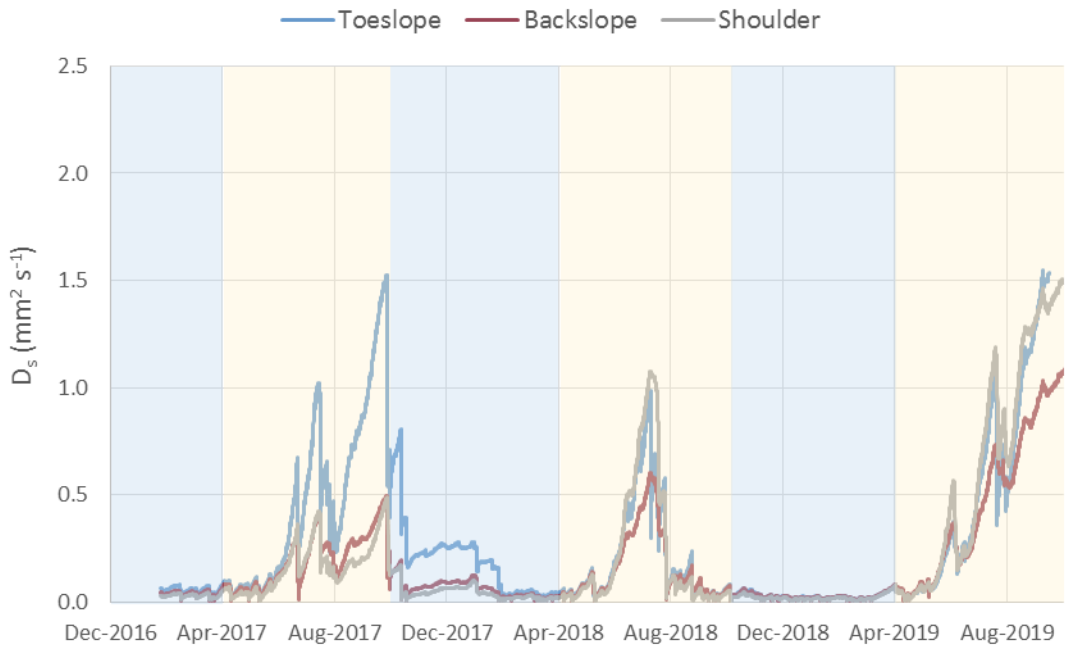

Figure 6. Calculated gas diffusivity, D_s (in mm^2 s^{-1}), for the three sinkhole slope locations. The cool seasons are indicated by the blue-shaded regions spanning from October through March and the warm seasons are indicated by the yellow shading spanning from April through September.

3.4.4 CO_2 fluxes

The shoulder hillslope soil profile had relatively large upward CO_2 fluxes and much smaller downward fluxes during the warm seasons (Figure 7). During the cool seasons, that profile had negligible upward and downward fluxes. The upward CO_2 fluxes peaked between 0.8 and 1.7 μmol CO_2 m^{-2} s^{-1}, while the downward fluxes never exceeded -0.7 μmol CO_2 m^{-2} s^{-1}.

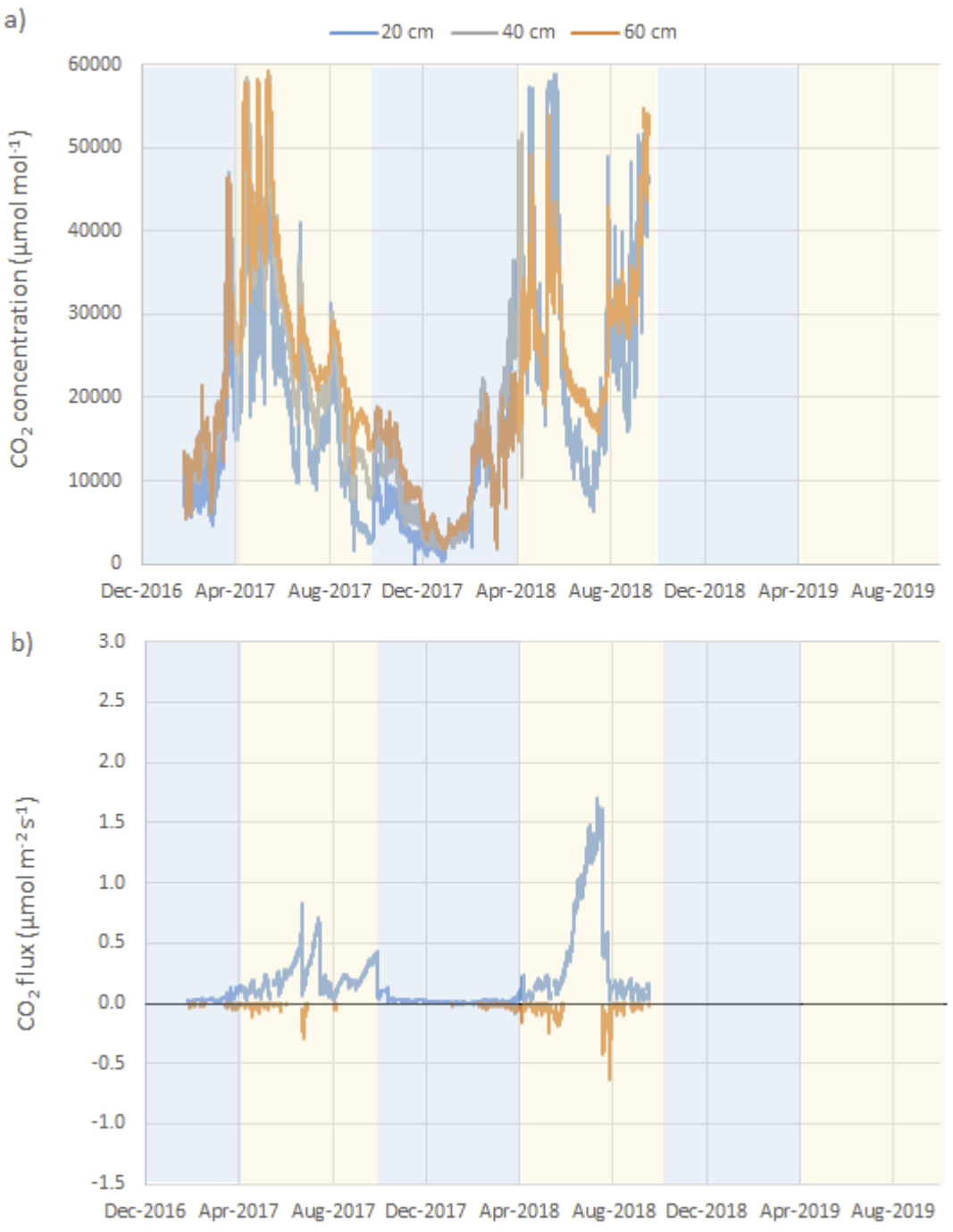

Figure 7. a) CO_2 concentrations at 20, 40, and 60 cm depths, and b) CO_2 flux in the shoulder location. The cool seasons are indicated by the blue-shaded regions spanning from October through March and warm seasons are indicated by yellow shading spanning from April through September. Due to CO_2 sensor failures, the data only extended through 24 September 2018.

The CO_2 flux for the backslope location had similar magnitudes of upward fluxes as the shoulder location (Figure 8). However, during the first warm season the downward fluxes were consistently larger than those detected in the shoulder profile. Furthermore, the downward and upward fluxes often had similar magnitude in this profile, with both directions showing larger values during warm seasons and near-zero values during the cool seasons.

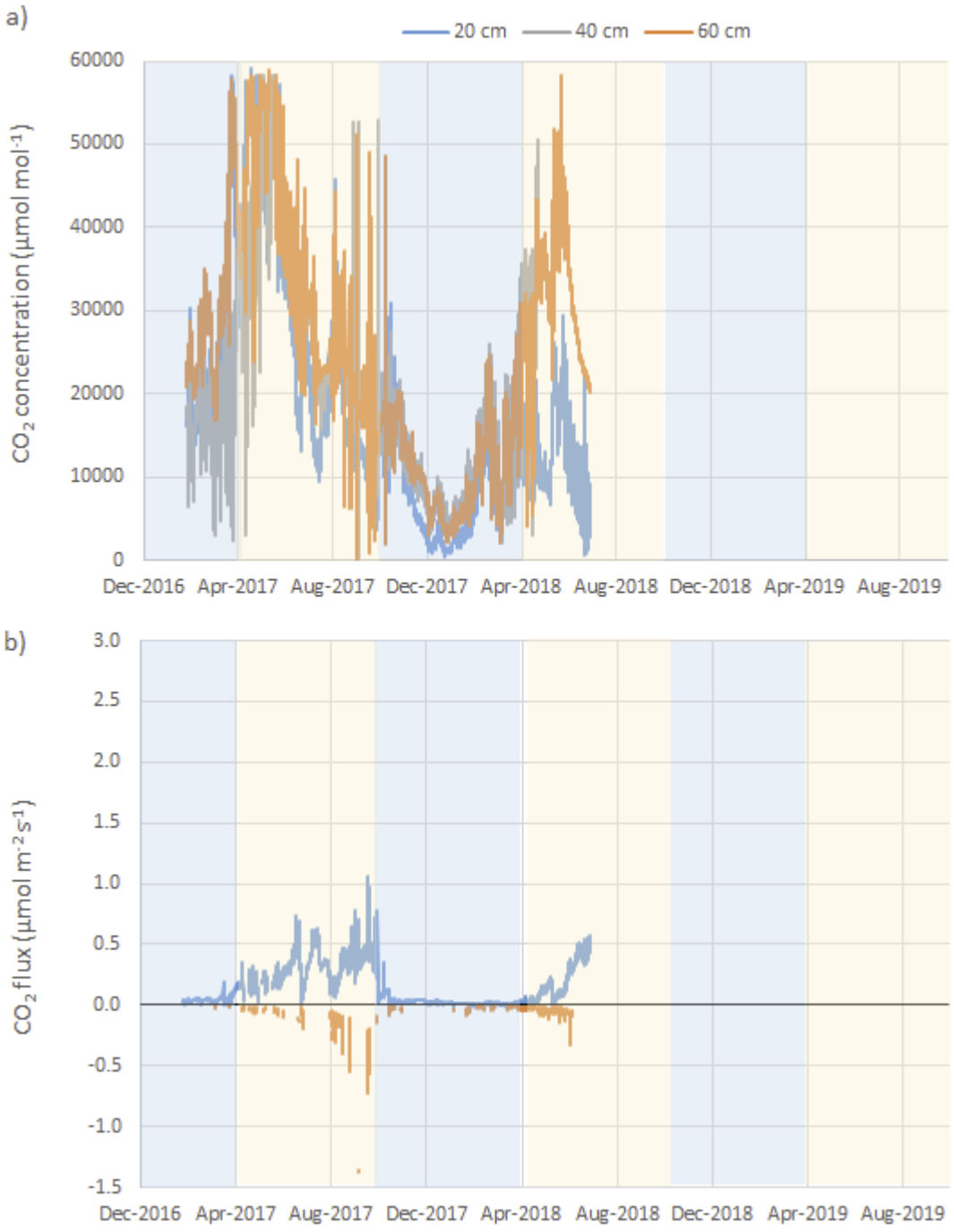

Figure 8. a) CO_2 concentrations at 20, 40, and 60 cm depths, and b) CO_2 flux in the backslope location. The cool seasons are indicated by the blue-shaded regions spanning from October through March and the warm seasons are indicated by the yellow shading spanning from April through September. Due to CO_2 sensor failures, the data only extends through 5 July 2018.

The toeslope location had consistently larger CO_2 fluxes than the other two profiles in both the upward and downward directions (Figure 9), reaching peaks of 2.4 μmol CO_2 m^{-2} s^{-1} (upward) and -1.5 μmol CO_2 m^{-2} s^{-1} (downward). Downward fluxes were only detected during the first half of the study, when the 40 cm sensor functioned, and were mainly identified during transitions between the cool and warm seasons.

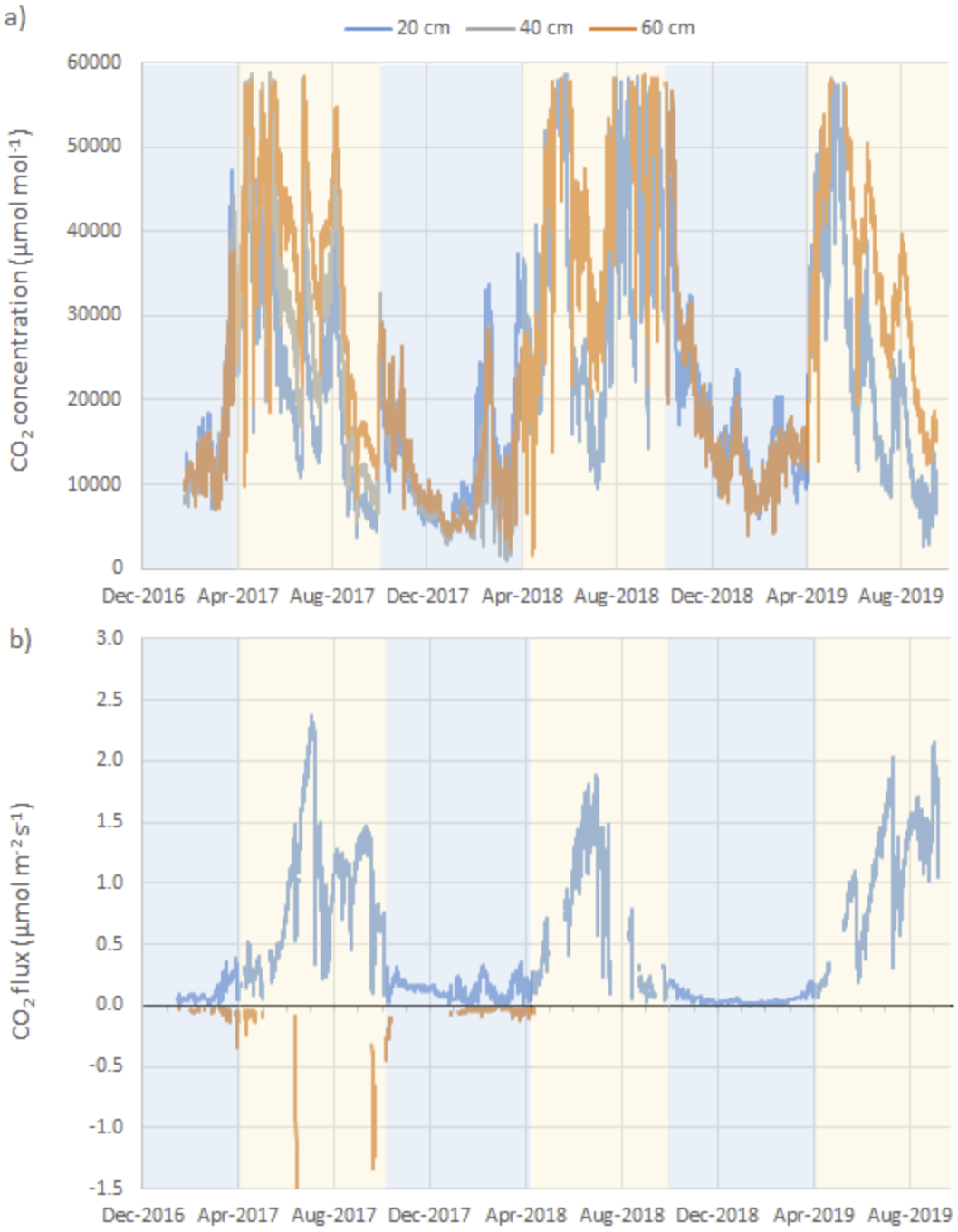

Figure 9. a) CO_2 concentrations at 20, 40, and 60 cm depths, and b) CO_2 flux in the toeslope location. The cool seasons are indicated by the blue-shaded regions spanning from October through March and the warm seasons are indicated by the yellow shading spanning from April through September.

Annual CO_2 efflux was calculated by integrating underneath the CO_2 flux curves for each profile from 1 April 2017 through 31 March 2018. Annual CO_2 efflux (i.e., upward flux) ranged from 3.9 mol CO_2 m^{-2} in the shoulder to 16.0 mol CO_2 m^{-2} in the toeslope (Table 2). Most of the efflux came during the warm period for all sinkhole slope locations, with warm season efflux representing between 78% (in the toeslope) to 86% (in the backslope) of total CO_2 emissions. The cumulative downward flux was much smaller, with the toeslope having a total of -0.60 mol CO_2 m^{-2}.

Table 2. Calculated cumulative CO_2 efflux for the three sinkhole slope positions over different time periods, in mol CO_2 m^{-2}. The annual period includes 1 April 2017 to 31 March 2018, the warm season includes 1 April 2017 to 30 September 2017, and the cool season includes 1 October 2017 to 31 March 2018.

		Cumulative Upward flux (mol CO_2 m^{-2})		
	# of Days	Shoulder	Backslope	Toeslope
Annual	365	3.93	4.97	16.0
Warm Season	183	3.32	4.25	12.4
Cool Season	182	0.61	0.72	3.53
		Cumulative Downward flux (mol CO_2 m^{-2})		
	# of Days	Shoulder	Backslope	Toeslope
Annual	365	-0.15	-0.26	-0.60
Warm Season	183	-0.10	-0.19	-0.22
Cool Season	182	-0.05	-0.07	-0.37

3.4.5 Sensitivity analysis

The sensitivity analysis revealed that the magnitude of D_s varied based on the assumed value of ϕ (Figure 10). Here the toeslope location was used as an example. Under the lowest tested ϕ value (0.40), the maximum D_s value was between 1.0 and 1.2 mm^2 s^{-1}. The largest tested ϕ value (0.56), gave a maximum D_s value of 2.8 mm^2 s^{-1}. In the cool season, when the soil water content was high, the variation in porosity drove the D_s value closer to zero for the minimum porosity

value and away from zero for the maximum porosity value. When ϕ = 0.44, the D_s term was near-zero for much of the cool season, versus 0.2-0.3 $mm^2\ s^{-1}$ when ϕ = 0.56.

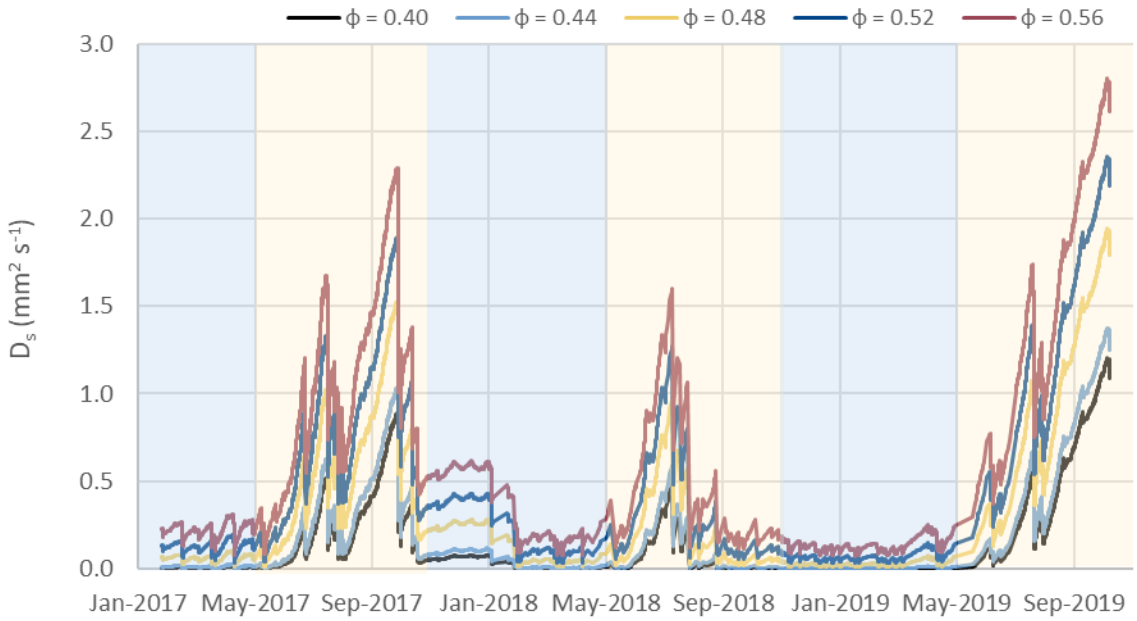

Figure 10. Calculated gas diffusivity, D_s, for the toeslope location assuming five different porosity values: ϕ = 0.40, 0.44, 0.48, 0.52, and 0.56 $cm^3\ cm^{-3}$. The cool seasons are indicated by the blue-shaded regions spanning from October through March and the warm seasons are indicated by the yellow shading spanning from April through September.

The differences in calculated D_s values translated to sizeable differences in the amount of CO_2 that was emitted from each soil profile over a one-year period (Figure 11). The relative differences were least in the toeslope location, with total CO_2 efflux varying by 6x between the lowest (ϕ = 0.40) and highest (ϕ = 0.56) porosities. The cumulative effluxes differed by 10x for the shoulder between the lowest and highest porosities. Relative differences were greatest in the backslope location, varying by 12x between the lowest and highest porosities.

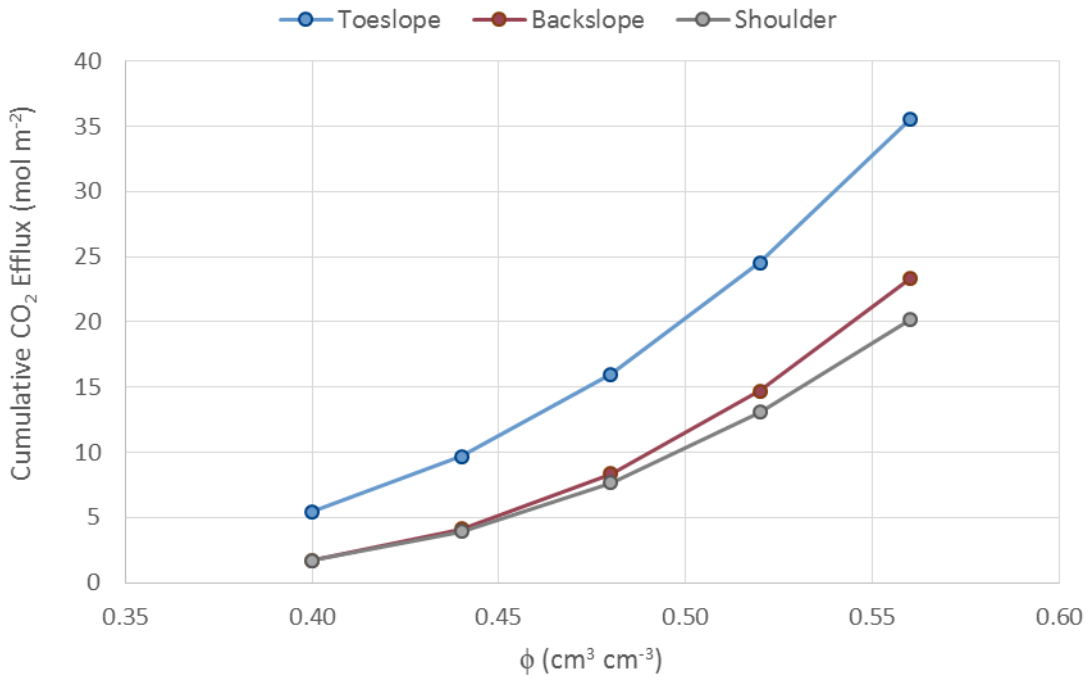

Figure 11. Sensitivity analysis showing calculated annual CO_2 efflux (in mol m^{-2}) between 1 April 2017 and 31 March 2018 for different porosity (ϕ) values.

3.5 Discussion

3.5.1 CO_2 fluxes

The objectives of this study were to 1) quantify spatial differences in CO_2 fluxes and 2) examine seasonal trends in CO_2 fluxes above a karst cave system. To address these objectives, I instrumented soil profiles at three sinkhole slope locations, including a shoulder, backslope, and toeslope.

My three hypotheses were 1) that the shoulder would have the largest upward CO_2 fluxes (i.e., CO_2 diffusing toward the soil surface) and smallest downward fluxes (i.e., CO_2 diffusing away from the soil surface), 2) that the toeslope would have larger downward CO_2 fluxes and relatively smaller upward fluxes, and 3) that CO_2 fluxes would be smaller and net downward during cooler months of the year and larger and net upward during warmer months of the year.

As discussed below, the results did not support my first two hypotheses, and provided partial support to my third hypothesis.

Across the entire study period, the three sinkhole slope positions exhibited similar behaviors in terms of the directions of CO_2 fluxes, but differed in their relative magnitude. More specifically, the backslope and shoulder profiles had smaller upward fluxes (peaking between around 1.0 μmol m^{-2} s^{-1}) than the toeslope profile (with peak fluxes of around 2.4 μmol m^{-2} s^{-1}). These efflux values were all considerably greater than that estimated using the gradient method in a non-karst soil (Tang et al., 2003), which showed consistent CO_2 fluxes of 0.35-0.40 μmol m^{-2} s^{-1} over a month-long period. That study also used solid-state sensors, yet they were installed at much shallower depths (2-16 cm). The fluxes within the Tang et al. (2003) study may have been lower than the flux estimates within this study due to climatic differences of Mediterranean climate with warm and dry conditions within the Tang et al. (2003) study with decreased amounts of precipitation within warmer months, potentially leading to lower efflux values within the Tang et al. (2003) study period as compared to this study.

In the first year of the study, the shoulder and backslope locations displayed similar upward CO_2 fluxes. These profiles tended to be wetter than the toeslope, particularly at the 20 and 40 cm depths, and those differences in water contents translated to smaller D_s values, and thus, limited efflux. However, during the second warm season (1 April 2018 – 22 September 2018), the shoulder became relatively dry, with the 20 and 60 cm depths displaying some of the lowest volumetric water contents recorded during the study. Consequently, the shoulder had the highest D_s values during this period, and the upward CO_2 fluxes were of greater magnitude than during the first year. The backslope location experienced the least amount of upward flux out of all

locations. This could be due to the backslope regularly displaying the lowest D_s values out of all profiles especially within the warm season months.

The toeslope location displayed larger upward fluxes compared to the two other profiles. During the first year, the toeslope profile displayed greater D_s values than the other locations, which was likely a factor causing the greater efflux. However, during the second warm season, the shoulder had similar D_s values as the toeslope, but the latter still had larger upward fluxes than the former (peak fluxes of 1.9 μmol m^{-2} s^{-1} in the toeslope versus 1.6 μmol m^{-2} s^{-1} in the shoulder). This difference suggests that the toeslope profile had more CO_2 production than the shoulder. Previous work in a snowmelt-dominant grassland system determined greater CO_2 efflux from a wetter riparian area than the surrounding uplands, even though D_s values were much larger in the latter (Pacific et al., 2008). Another study working in grazed pastures determined that slope angle affects carbon allocation, with grasses growing on flatter slopes having greater respiration than those growing on steep slopes (Saggar et al., 1999). The smaller magnitude CO_2 fluxes observed in the backslope location – and to a lesser extent the shoulder – suggest that slope may also affect carbon uptake and respiration by grasses in this karst landscape.

The downward diffusion of CO_2 gas towards underlying karst layers (i.e., epikarst and cave system) also may have affected CO_2 efflux from the soil surface. The downward CO_2 fluxes were of greater magnitude during the warmer months than the cooler months, particularly in the shoulder and backslope locations. The cave system may be responsible for the larger downward CO_2 fluxes during the warm season for the shoulder and backslope locations. Previous work has identified cave gas venting through the overlying soil profile during dry periods of the year, when soil air-filled porosity is sufficient to enable rapid gas diffusion rates (Sanchez-Cañete et al., 2011; Cuezva et al., 2011; Weisbrod et al., 2009; Fernandez-Cortes et al., 2011). The periods

of downward CO_2 flux during the growing season suggests that process may have acted in reverse in this system. At the same time, measured soil CO_2 concentrations often exceeded 40,000 ppmv (4%) during the growing season. While we did not directly measure CO_2 concentrations in the cave, other work in similar caves has measured concentrations ranging from 5,000 to 20,000 ppmv. Therefore, it is possible that downward diffusion may have occurred below the deepest sensor (60 cm) during the growing seasons, and as a result the instantaneous and cumulative downward fluxes were under-estimated here.

Both upward and downward CO_2 fluxes demonstrated seasonal patterns. Upward fluxes were larger and more consistent during the warm growing season, when soil temperatures were warm (18 to 25°C), likely causing greater autotrophic and heterotrophic respiration with increase in temperature (Ali et al., 2018). With only a few exceptions, downward fluxes were not seen during the periods of large upward fluxes. This pattern was different in the cool season, where limited CO_2 production and lower D_s values likely limited the upward efflux while downward fluxes were frequently observed. The downward fluxes tended to be small in magnitude, with the largest magnitudes observed in the spring transition (e.g., February to June).

Other studies in temperate regions have shown that cave ventilation increases during the winter period, as natural convection allows warmer cave air to escape via cave openings and become replaced by atmospheric air that is low in CO_2 (Krajnc et al., 2017; Mattey et al., 2016). Under such conditions, CO_2 concentrations in the soil would be elevated, driving downward diffusion, so long as the gas diffusivity was sufficient. The toeslope location was also the closest in elevation to the cave system. Thus, proximity may also play a role in influencing downward diffusion within soil profiles relative to the cave system.

Another potential influence driving downward diffusion from the soil profile during the cooler months, especially at the toeslope location, could be the weathering of carbonate rocks, as CO_2 becomes converted into carbonic acid (H_2CO_3) and then bicarbonate (HCO_3^-) (Fang et al., 2012). This weathering process likely led to an increase in consumed CO_2 moving through the epikarst and into the cave system via infiltrating water. This process is highly seasonal, with increased CO_2 consumption identified during December to March, when James Cave and other similar systems typically begin to experience aquifer recharge via cave drips (Eagle et al., 2015). This process has previously been correlated with decreased CO_2 concentrations at depth (Benavente et al., 2010; Chen, 2019), which would create the potential for downward CO_2 diffusion toward the epikarst and karstic layers.

Other studies (e.g., Yang et al., 2012) have indicated similar seasonal patterns as measured here, such as increasing soil CO_2 concentrations during the growing season followed by decreased concentrations during the dormant season. However, many of these studies did not measure CO_2 concentrations at multiple depths (Bergel et al., 2017; Blecha & Faimon, 2014; Cao et al., 2020; Lang & Faimon, 2020; Lopez et al., 2018; Mattey et al., 2016; Sanchez-Cañete et al., 2011), and therefore were unable to assess the direction and magnitude of CO_2 diffusion in karst soils. Some other studies did measure CO_2 concentrations at multiple depths (Benavente et al., 2010; Breecker et al., 2012; Chen, 2019; Crowther, 1984; Fang et al., 2012; Krajnc et al., 2017), but only compared relative CO_2 concentrations by depth or focused their analysis on comparing CO_2 concentrations with other variables such as temperature, water content, organic carbon allocation, and cave ventilation. Therefore, the analysis of direction of CO_2 diffusion in karst soils is one of the unique features of the present study.

3.5.2 Sensitivity Analysis

The CO_2 fluxes calculated in this study were sensitive to the assumed porosity value. Previous work has shown that air-filled porosity is one of the most important terms for D_s (Lafond et al., 2011; Jin & Jury, 1996), which was reflected in the diffusion model used here (Equations 3-5). In this study, porosity values were based on measurements taken from soil cores, in an attempt to reduce uncertainty associated with that parameter. Nonetheless, the measured porosity values varied between cores (from 0.40 to 0.55 cm^3 cm^{-3}), while the actual porosity in the field likely differed from the values measured from the cores, and also by depth. Altogether these factors increased the uncertainty of calculated CO_2 fluxes in this study.

At the same time, other measurements and models for D_s have identified the importance of larger macropores for gas diffusion (Jayarathne et al., 2020). Most of the water retention curves collected on the soil samples showed sizeable differences in water content between saturation and field capacity (e.g., 0.10 – 0.15 cm^3 cm^{-3}), which can be an indication of the volume of easily drained macropores and mesopores in a soil (i.e., pores > 10 μm in size; Luxmoore, 1981). Likewise, highly weathered epikarst layers that lie beneath the soil mantle often contain many fractures and large pores (Weisbrod et al., 2009; Mattey et al., 2016; Cao et al., 2020; Eagle et al., 2015; White, 2016), which could act as conduits for subsurface diffusion if conditions allowed. Therefore, future work may focus on better understanding how spatial differences in vadose zone properties – including total soil porosity, soil macroporosity, and epikarst fracture connectivity – influence D_s values and gas diffusion rates.

3.5.3 Limitations of the study

The study had several limitations. For instance, many of the solid-state sensors reached maximum readings (5.5%) multiple times during the study, which resulted in data gaps. Moreover, many of the sensors started to fail after 1.5-2.5 years, affecting the duration of the observational record.

Most of the initial failures occurred at sensors that were installed at the 40 cm depth, limiting my ability to identify zero-flux planes when the maximum CO_2 concentrations were located at depth.

At the same time, the overall spacing between sensors in this study was large compared to other studies (e.g., 8 cm spacing in Tang et al., 2003), which increased the likelihood that the concentration gradients were not uniform between sensors. The shallowest sensor depth was at 20 cm, deeper than installed sensor depths within other studies (e.g., 5 cm depth in Lopez et al., 2018) potentially limiting the accuracy of the calculated CO_2 flux between the atmosphere and the shallowest sensor depth of 20 cm. Calculated efflux between the measured CO_2 concentration at the 20 cm depth and the assumed atmospheric concentration could have been underestimated, if there were greater CO_2 concentrations at depths shallower than 20 cm.

The study was also limited in its spatial extent and lack of any measurements within the deeper epikarst or cave system. The characterization of deeper zero-flux planes could be possible with the installation of CO_2 sensors at depth > 60 cm. Carbon isotopic discrimination techniques could also be used to trace the sources and dynamics of carbon movement deeper within the subsurface (Breecker et al., 2012; Mattey et al., 2016). Both of these methods would aid in identifying carbon dynamics deeper into the epikarstic and karstic zones. Despite installing sensors deeper than many other studies, the deepest (60 cm) sensor was still positioned well above the epikarst layers. Future studies should strive to incorporate concurrent CO_2 measurements from soils that surround cave systems (Mattey et al., 2016), rather than study each system in isolation as the soil profile (Benavente et al., 2010; Chen, 2019) and cave system separately (Faimon et al., 2012).

Finally, due to limitations in materials and budget, the study was limited to a single site, with only one set of sensors per sinkhole slope position. The lack of replication prevented statistical comparisons both between the different soil profiles as well as with other sinkholes. Nonetheless,

the common seasonal patterns measured in all three profiles suggests that the sensors were adequately capturing CO_2 dynamics within the sinkhole. Similarly, doline caves like James Cave commonly occur throughout southwest Virginia and the larger eastern United States. Therefore, the findings of this study should be generalizable to other karst areas in the region with similar geologic and environmental factors.

4. References

Ali, R. S., Poll, C., & Kandeler, E. (2018). Dynamics of soil respiration and microbial communities: Interactive controls of temperature and substrate quality. *Soil Biology and Biochemistry*, *127*, 60–70. https://doi.org/10.1016/j.soilbio.2018.09.010

Allaire, S. E., Lafond, J. A., Cabral, A. R., & Lange, S. F. (2008). Measurement of gas diffusion through soils: Comparison of laboratory methods. *Journal of Environmental Monitoring*, *10*(11), 1326–1336. https://doi.org/10.1039/b809461f

Benavente, J., Vadillo, I., Carrasco, F., Soler, A., Liñán, C., & Moral, F. (2010). Air carbon dioxide contents in the vadose zone of a Mediterranean Karst. *Vadose Zone Journal*, *9*(1), 126–136. https://doi.org/10.2136/vzj2009.0027

Bergel, S. J., Carlson, P. E., Larson, T. E., Wood, C. T., Johnson, K. R., Banner, J. L., & Breeker, D. O. (2017). Constraining the subsoil carbon source to cave-air CO_2 and speleothem calcite in Central Texas. *Geochimica et Cosmochimica Acta*, *217*, 112–127. https://doi.org/10.1016/j.gca.2017.08.017

Beven, K., & Germann, P. (1982). Macropores and water flow in soils. *Water Resources Research*, *18*(5), 1311–1325. https://doi.org/10.1029/WR018i005p01311

Blecha, M., & Faimon, J. (2014). Spatial and temporal variations in carbon dioxide (CO_2) concentrations in selected soils of the Moravian Karst (Czech Republic). *Carbonates and Evaporites*, *29*(4), 395–408. https://doi.org/10.1007/s13146-014-0220-7

Bond-Lamberty, B., & Thomson, A. (2010). Temperature-associated increases in the global soil respiration record. *Nature*, *464*(7288), 579–582. https://doi.org/10.1038/nature08930

Breecker, D. O., Payne, A. E., Quade, J., Banner, J. L., Ball, C. E., Meyer, K. W., & Cowan, B. D. (2012). The sources and sinks of CO_2 in caves under mixed woodland and grassland vegetation. *Geochimica et Cosmochimica Acta*, *96*, 230–246. https://doi.org/10.1016/j.gca.2012.08.023

Brown, R., & Markewitz, D. (2018). Soil heterotrophic respiration: Measuring and modeling seasonal variation and silvicultural impacts. *Forest Ecology and Management*, *430*, 594–608. https://doi.org/10.1016/j.foreco.2018.08.018

Brutsaert, W. (2014). The daily mean zero-flux plane during soil-controlled evaporation: A Green's function approach. *Water Resources Research*, *50*(12), 9405–9413. https://doi.org/10.1002/2014WR016111

Cao, M., Jiang, Y., Chen, Y., Fan, J., & He, Q. (2020). Variations of soil CO_2 concentration and pCO_2 in a cave stream on different time scales in subtropical climatic regime. *CATENA*, *185*(104280), 1–15. https://doi.org/10.1016/j.catena.2019.104280

Chen, Q. (2019). Characteristics of soil profile CO_2; concentrations in karst areas and their significance for global carbon cycles and climate change. *Earth System Dynamics*, *10*(3), 525–538. https://doi.org/10.5194/esd-10-525-2019

Crowther, J. (1984). Soil carbon dioxide and weathering potentials in tropical karst terrain, peninsular Malaysia: A preliminary model. *Earth Surface Processes and Landforms*, *9*(5), 397–407. https://doi.org/10.1002/esp.3290090502

Cueva, A., Bahn, M., Litvak, M., Pumpanen, J., & Vargas, R. (2015). A multisite analysis of temporal random errors in soil CO_2 efflux. *Journal of Geophysical Research: Biogeosciences*, *120*(4), 737–751. https://doi.org/10.1002/2014JG002690

Cuezva, S., Fernandez-Cortes, A., Benavente, D., Serrano-Ortiz, P., Kowalski, A. S., & Sanchez-Moral, S. (2011). Short-term CO_2 (g) exchange between a shallow karstic cavity and the external atmosphere during summer: Role of the surface soil layer. *Atmospheric Environment*, *45*(7), 1418–1427. https://doi.org/10.1016/j.atmosenv.2010.12.023

Di Prima, S., Giannini, V., Ribeiro Roder, L., Giadrossich, F., Lassabatere, L., Stewart, R. D., Abou Najm, M. R., Longo, V., Campus, S., Winiarski, T., Angulo-Jaramillo, R., del Campo, A., Capello, G., Biddoccu, M., Roggero, P. P., & Pirastru, M. (2021). Coupling time-lapse ground penetrating radar surveys and infiltration experiments to characterize two types of non-uniform flow. *Science of The Total Environment*, *806*(150410), 1–10. https://doi.org/10.1016/j.scitotenv.2021.150410

Eagle, S., Orndorff, W., Schwartz, B., Doctor, D. H., Gerst, J., & Schreiber, M. (2015). Analysis of hydrologic and geochemical time-series data at James Cave, Virginia: Implications for epikarst influence on recharge in Appalachian karst aquifers. *Geological Society of America Special Papers 516*, 181–196. https://doi.org/10.1130/2015.2516(15)

Fa, K.-Y., Liu, J.-B., Zhang, Y.-Q., Wu, B., Qin, S.-G., Feng, W., & Lai, Z.-R. (2015). CO_2 absorption of sandy soil induced by rainfall pulses in a desert ecosystem. *Hydrological Processes*, *29*(8), 2043–2051. https://doi.org/10.1002/hyp.10350

Faimon, J., Troppová, D., Baldík, V., & Novotný, R. (2012). Air circulation and its impact on microclimatic variables in the Císařská Cave (Moravian Karst, Czech Republic). *International Journal of Climatology*, *32*(4), 599–623. https://doi.org/10.1002/joc.2298

Fan, J., & Jones, S. B. (2014). Soil surface wetting effects on gradient-based estimates of soil carbon dioxide efflux. *Vadose Zone Journal*, *13*(2), 1–12. https://doi.org/10.2136/vzj2013.07.0124

Fang, C. & Moncrieff, J. B. (2005). The variation of soil microbial respiration with depth in relation to soil carbon composition. *Plant and Soil*, *268*, 243–253. https://doi.org/10.1007/s11104-004-0278-4

Fang, L., Cong-Qiang, L., Shi-lu, W., & Zheng-jie, Z. (2012). Soil temperature and moisture controls on surface fluxes and profile concentrations of greenhouse gases in karst area in central part of Guizhou Province, Southwest China. *Environmental Earth Sciences*, *67*(5), 1431–1439. https://doi.org/10.1007/s12665-012-1588-0

Farmer, W. J., Igue, K., & Spencer, W. F. (1973). Effect of bulk density on the diffusion and volatilization of dieldrin from soil. *Journal Environmental Quality*, *2*(1), 107–109.

Fernandez-Cortes, A., Sanchez-Moral, S., Cuezva, S., Benavente, D., & Abella, R. (2011). Characterization of trace gases' fluctuations on a 'low energy' cave (Castañar de Íbor, Spain) using techniques of entropy of curves. *International Journal of Climatology*, *31*(1), 127–143. https://doi.org/10.1002/joc.2057

Ford, D., & Williams, P. (2007). *Karst Hydrogeology and Geomorphology*. John Wiley & Sons Ltd.

Fujikawa, T., & Miyazaki, T. (2005). Effects of bulk density and soil type on the gas diffusion coefficient in repacked and undisturbed soils. *Soil Science*, *170*(11), 892–901. https://doi.org/10.1097/01.ss.0000196771.53574.79

Groce-Wright, N. C. (2021). *Analyzing a 10-Year Cave Drip Record in James Cave, Virginia: Implications for Storage and Recharge in Shallow Appalachian Karst Systems*. (Master's Thesis). 1–46.

Hillel, D. (2003). Gas Movement and Exchange. In *Introduction to Environmental Soil Physics* (pp. 201–212). Elsevier. https://doi.org/10.1016/B978-0-12-348655-4.X5000-X

Iiyama, I., & Hasegawa, S. (2005). Gas diffusion coefficient of undisturbed peat soils. *Soil Science and Plant Nutrition*, *51*(3), 431–435. https://doi.org/10.1111/j.1747-0765.2005.tb00049.x

Jackisch, C., Angermann, L., Allroggen, N., Sprenger, M., Blume, T., Tronicke, J., & Zehe, E. (2017). Form and function in hillslope hydrology: In situ imaging and characterization of flow-relevant structures. *Hydrology and Earth System Sciences*, *21*(7), 3749–3775. https://doi.org/10.5194/hess-21-3749-2017

Jassal, R., Black, A., Novak, M., Morgenstern, K., Nesic, Z., & Gaumont-Guay, D. (2005). Relationship between soil CO_2 concentrations and forest-floor CO_2 effluxes. *Agricultural and Forest Meteorology*, *130*, 176–192. https://doi.org/10.1016/j.agrformet.2005.03.005

Jayarathne, J. R. R. N., Chamindu Deepagoda, T. K. K., Clough, T. J., Nasvi, M. C. M., Thomas, S., Elberling, B., & Smits, K. (2020). Gas-diffusivity based characterization of aggregated agricultural soils. *Soil Science Society of America Journal*, *84*(2), 387–398. https://doi.org/10.1002/saj2.20033

Jiang, Y., Lei, J., Hu, L., Xiao, Q., Wang, J., Zhang, C., & Ali, H. (2020). Biogeochemical and physical controls on the evolution of dissolved inorganic carbon (DIC) and $\delta^{13}C$ DIC in karst spring-waters exposed to atmospheric CO_2 (g): Insights from laboratory experiments. *Journal of Hydrology*, *583*, 124-294. https://doi.org/10.1016/j.jhydrol.2019.124294

Jin, Y., & Jury, W. A. (1996). Characterizing the dependence of gas diffusion coefficient on soil properties. *Soil Science Society of America Journal*, *60*(1), 66–71. https://doi.org/10.2136/sssaj1996.03615995006000010012x

Jong, E. D., & Schappert, H. J. V. (1972). Calculation of soil respiration and activity from CO_2 profiles in the soil. *Soil Science*, *113*(5), 328–333. https://doi.org/10.1097/00010694-197205000-00006

Kaspar, T. C., & Parkin, T. B. (2011). Soil carbon dioxide flux in response to wheel traffic in a no-till system. *Soil Science Society of America Journal*, *75*(6), 2296–2304. https://doi.org/10.2136/sssaj2011.0129

Khalil, M., Sakai, M., Mizoguchi, M., & Miyazaki, T. (2003). Current and prospective applications of zero flux plane (ZFP) method. *Journal of the Japanese Society of Soil Physics*, *95*, 75–90.

Kiefer, R. H. (1990). Soil carbon dioxide concentrations and climate in a humid subtropical environment. *The Professional Geographer*, *42*(2), 182–194. https://doi.org/10.1111/j.0033-0124.1990.00182.x

Krajnc, B., Ferlan, M., & Ogrinc, N. (2017). Soil CO_2 sources above a subterranean cave—Pisani rov (Postojna Cave, Slovenia). *Journal of Soils and Sediments*, *17*(7), 1883–1892. https://doi.org/10.1007/s11368-016-1543-x

Kristensen, A. H., Thorbjørn, A., Jensen, M. P., Pedersen, M., & Moldrup, P. (2010). Gas-phase diffusivity and tortuosity of structured soils. *Journal of Contaminant Hydrology*, *115*, 26–33. https://doi.org/10.1016/j.jconhyd.2010.03.003

Kutsch, W., Bahn, M., & Heinemeyer, A. (Eds.). (2009). *Soil Carbon Dynamics: An Integrated Methodology*. Cambridge University Press.

Laemmel, T., Maier, M., Schack-Kirchner, H., & Lang, F. (2017). An in situ method for real-time measurement of gas transport in soil: Monitoring of gas transport in soil. *European Journal of Soil Science*, *68*(2), 156–166. https://doi.org/10.1111/ejss.12412

Lafond, J. A., Allaire, S. E., Dutilleul, P., Pelletier, B., Lange, S. F., & Cambouris, A. N. (2011). Spatiotemporal analysis of the relative soil gas diffusion coefficient in two sandy soils: Variability decomposition and correlations between sampling dates at two spatial scales. *Soil Science Society of America Journal*, *75*(5), 1613–1625. https://doi.org/10.2136/sssaj2010.0419

Lang, M., & Faimon, J. (2020). Effect of water excess on soil carbon dioxide, seepage water chemistry, and calcite speleothem growth: An experimental and modelling approach. *Hydrological Processes*, *34*(22), 4334–4349. https://doi.org/10.1002/hyp.13877

Liu, J., Feng, W., Zhang, Y., Jia, X., Wu, B., Qin, S., Fa, K., & Lai, Z. (2015). Abiotic CO_2 exchange between soil and atmosphere and its response to temperature. *Environmental Earth Sciences*, *73*(5), 2463–2471. https://doi.org/10.1007/s12665-014-3595-9

Lopez, C. J. R., Sánchez-Cañete, E. P., Serrano-Ortiz, P., López-Ballesteros, A., Domingo, F., Kowalski, A. S., & Oyonarte, C. (2018). From microhabitat to ecosystem: Identifying the biophysical factors controlling soil CO_2 dynamics in a karst shrubland: Biophysical factors controlling soil CO_2 dynamics. *European Journal of Soil Science*, *69*(6), 1018–1029. https://doi.org/10.1111/ejss.12710

Luther-Mosebach, J., Kalinski, K., Gröngröft, A., & Eschenbach, A. (2018). CO_2 fluxes in subtropical dryland soils: A comparison of the gradient and the closed-chamber method.

Journal of Plant Nutrition and Soil Science, *181*(1), 21–30. https://doi.org/10.1002/jpln.201600137

Luxmoore, R. J. (1981). Micro-, Meso-, and Macroporosity of Soil. *Soil Science Society of America Journal*, *45*(3), 671–672. https://doi.org/10.2136/sssaj1981.03615995004500030051x

Maier, M., & Schack-Kirchner, H. (2014). Using the gradient method to determine soil gas flux: A review. *Agricultural and Forest Meteorology*, *192–193*, 78–95. https://doi.org/10.1016/j.agrformet.2014.03.006

Mattey, D. P., Atkinson, T. C., Barker, J. A., Fisher, R., Latin, J.-P., Durrell, R., & Ainsworth, M. (2016). Carbon dioxide, ground air and carbon cycling in Gibraltar karst. *Geochimica et Cosmochimica Acta*, *184*, 88–113. https://doi.org/10.1016/j.gca.2016.01.041

Moldrup, P., Olesen, T., Schjønning, P., Yamaguchi, T., & Rolston, D. E. (2000). Predicting the gas diffusion coefficient in undisturbed soil from soil water characteristics. *Soil Science Society of America Journal*, *64*(1), 94–100. https://doi.org/10.2136/sssaj2000.64194x

Moldrup, P., Olesen, T., Yoshikawa, S., Komatsu, T., & Rolston, D. E. (2004). Three-porosity model for predicting the gas diffusion coefficient in undisturbed soil. *Soil Science Society of America Journal*, *68*(3), 750–759. https://doi.org/10.2136/sssaj2004.7500

Pacific, V. J., McGlynn, B. L., Riveros-Iregui, D. A., Welsch, D. L., & Epstein, H. E. (2008). Variability in soil respiration across riparian-hillslope transitions. *Biogeochemistry*, *91*(1), 51–70. https://doi.org/10.1007/s10533-008-9258-8

Peng, S., Hu, Q., & Hamamoto, S. (2012). Diffusivity of rocks: Gas diffusion measurements and correlation to porosity and pore size distribution. *Water Resources Research*, *48*(2), 1–9. https://doi.org/10.1029/2011WR011098

Pingintha, N., Leclerc, M., Beasley, J., Zhang, G., & Senthong, C. (2010). Assessment of the soil CO_2 gradient method for soil CO_2 efflux measurements: Comparison of six models in the calculation of the relative gas diffusion coefficient. *Tellus B: Chemical and Physical Meteorology*, *62*(1), 47–58. https://doi.org/10.1111/j.1600-0889.2009.00445.x

Pumpanen, J., Ilvesniemi, H., & Hari, P. (2003). A process-based model for predicting soil carbon dioxide efflux and concentration. *Soil Science Society of America Journal*, *67*(2), 402–413. https://doi.org/10.2136/sssaj2003.4020

Raich, J. W., & Potter, C. S. (1995). Global patterns of carbon dioxide emissions from soils. *Global Biogeochemical Cycles*, *9*(1), 23–36. https://doi.org/10.1029/94GB02723

Raich, J. W., & Schlesinger, W. H. (1992). The global carbon dioxide flux in soil respiration and its relationship to vegetation and climate. *Tellus B*, *44*(2), 81–99. https://doi.org/10.1034/j.1600-0889.1992.t01-1-00001.x

Reicosky, D. C., & Lindstrom, M. J. (1993). Fall tillage method: Effect on short-term carbon dioxide flux from soil. *Agronomy Journal*, *85*(6), 1237–1243. https://doi.org/10.2134/agronj1993.00021962008500060027x

Rey, A. (2015). Mind the gap: Non-biological processes contributing to soil CO_2 efflux. *Global Change Biology*, *21*(5), 1752–1761. https://doi.org/10.1111/gcb.12821

Risk, D., Kellman, L., & Beltrami, H. (2002). Carbon dioxide in soil profiles: Production and temperature dependence. *Geophysical Research Letters*, *29*(6), 11-1–11-4. https://doi.org/10.1029/2001GL014002

Saggar, S., Mackay, A. D., & Hedley, C. B. (1999). Hillslope effects on the vertical fluxes of photosynthetically fixed ^{14}C in a grazed pasture. *Soil Research*, *37*(4), 655-666. https://doi.org/10.1071/SR98114

Sánchez-Cañete, E. P., Oyonarte, C., Serrano-Ortiz, P., Curiel Yuste, J., Pérez-Priego, O., Domingo, F., & Kowalski, A. S. (2016). Winds induce CO_2 exchange with the atmosphere and vadose zone transport in a karstic ecosystem: Dynamics of CO_2 within the vadose zone. *Journal of Geophysical Research: Biogeosciences*, *121*(8), 2049–2063. https://doi.org/10.1002/2016JG003500

Sánchez-Cañete, E. P., Scott, R. L., van Haren, J., & Barron-Gafford, G. A. (2017). Improving the accuracy of the gradient method for determining soil carbon dioxide efflux: Accurate long-term F_{soil} based on the GM. *Journal of Geophysical Research: Biogeosciences*, *122*(1), 50–64. https://doi.org/10.1002/2016JG003530

Sanchez-Cañete, E. P., Serrano-Ortiz, P., Kowalski, A. S., Oyonarte, C., & Domingo, F. (2011). Subterranean CO_2 ventilation and its role in the net ecosystem carbon balance of a karstic shrubland. *Geophysical Research Letters 38*(9), 1–4. http://doi.wiley.com/10.1029/2011GL047077

Schjønning, P., Eden, M., Moldrup, P., & de Jonge, L. W. (2013). Two-chamber, two-gas and one-chamber, one-gas methods for measuring the soil-gas diffusion coefficient: Validation and inter-calibration. *Soil Science Society of America Journal*, *77*(3), 729–740. https://doi.org/10.2136/sssaj2012.0379

Schlesinger, W. H. (1986). Changes in Soil Carbon Storage and Associated Properties with Disturbance and Recovery. In J. R. Trabalka & D. E. Reichle (Eds.), *The Changing Carbon Cycle* (pp. 194–220). Springer New York. https://doi.org/10.1007/978-1-4757-1915-4_11

Schreiber, M. E., Schwartz, B. F., Orndorff, W., Doctor, D. H., Eagle, S. D., & Gerst, J. D. (2015). Instrumenting caves to collect hydrologic and geochemical data: Case study from James Cave, Virginia. In T. Younos & T. E. Parece (Eds.), *Advances in Watershed Science and Assessment* (Vol. 33, pp. 205–231). Springer International Publishing. https://doi.org/10.1007/978-3-319-14212-8_8

Serrano-Ortiz, P., Roland, M., Sanchez-Moral, S., Janssens, I. A., Domingo, F., Goddéris, Y., & Kowalski, A. S. (2010). Hidden, abiotic CO_2 flows and gaseous reservoirs in the terrestrial carbon cycle: Review and perspectives. *Agricultural and Forest Meteorology*, *150*(3), 321–329. https://doi.org/10.1016/j.agrformet.2010.01.002

Shcherbak, I., & Philip Robertson, G. (2014). Determining the diffusivity of nitrous oxide in soil using in situ tracers. *Soil Science Society of America Journal*, *78*(1), 79–88. https://doi.org/10.2136/sssaj2013.05.0181

Shi, W.-Y., Zhang, J.-G., Yan, M.-J., Yamanaka, N., & Du, S. (2012). Seasonal and diurnal dynamics of soil respiration fluxes in two typical forests on the semiarid Loess Plateau of China: Temperature sensitivities of autotrophs and heterotrophs and analyses of integrated driving factors. *Soil Biology and Biochemistry*, *52*, 99–107. https://doi.org/10.1016/j.soilbio.2012.04.020

So, H. B., & Nye, P. H. (1989). The effect of bulk density, water content and soil type on the diffusion of chloride in soil. *Journal of Soil Science*, *40*(4), 743–749. https://doi.org/10.1111/j.1365-2389.1989.tb01314.x

Tang, J., Baldocchi, D. D., Qi, Y., & Xu, L. (2003). Assessing soil CO_2 efflux using continuous measurements of CO_2 profiles in soils with small solid-state sensors. *Agricultural and Forest Meteorology*, *118*, 207–220. https://doi.org/10.1016/S0168-1923(03)00112-6

Trinh, D. A., Trinh, Q. H., Fernandez-Cortes, A., Mattey, D., & Guinea, J. G. (2018). First assessment on the air CO_2 dynamic in the show caves of tropical karst, Vietnam. *International Journal of Speleology*, *47*(1), 93–112. https://doi.org/10.5038/1827-806X.47.1.2141

Trivedi, P., Singh, B. P., & Singh, B. K. (2018). Soil carbon. In *Soil Carbon Storage* (pp. 1–28). Elsevier. https://doi.org/10.1016/B978-0-12-812766-7.00001-9

Turcu, V. E., Jones, S. B., & Or, D. (2005). Continuous soil carbon dioxide and oxygen measurements and estimation of gradient-based gaseous flux. *Vadose Zone Journal*, *4*(4), 1161–1169. https://doi.org/10.2136/vzj2004.0164

van Genuchten, M. Th. (1980). A closed-form equation for predicting the hydraulic conductivity of unsaturated soils. *Soil Science Society of America Journal*, *44*(5), 892–898. https://doi.org/10.2136/sssaj1980.03615995004400050002x

Vaisala Application Note – CO_2 Measurement in Incubators - Questions and Answers-B210826EN-B. (2017). *Vaisala*.

Vargas, R., Baldocchi, D. D., Allen, M. F., Bahn, M., Black, T. A., Collins, S. L., Yuste, J. C., Hirano, T., Jassal, R. S., Pumpanen, J., & Tang, J. (2010). Looking deeper into the soil: Biophysical controls and seasonal lags of soil CO_2 production and efflux. *Ecological Applications*, *20*(6), 1569–1582. https://doi.org/10.1890/09-0693.1

Villegas, A. N., & Morris, R. A. (1990). Zero flux plane recession under monocropped and intercropped cowpea and sorghum. *Agronomy Journal*, *82*(4), 845–851. https://doi.org/10.2134/agronj1990.00021962008200040036x

Wan, J., Tokunaga, T. K., Williams, K. H., Dong, W., Brown, W., Henderson, A. N., Newman, A. W., & Hubbard, S. S. (2019). Predicting sedimentary bedrock subsurface weathering fronts and weathering rates. *Scientific Reports*, *9*(17198), 1–10. https://doi.org/10.1038/s41598-019-53205-2

Wanyama, I., Pelster, D. E., Butterbach-Bahl, K., Verchot, L. V., Martius, C., & Rufino, M. C. (2019). Soil carbon dioxide and methane fluxes from forests and other land use types in an African tropical montane region. *Biogeochemistry*, *143*(2), 171–190. https://doi.org/10.1007/s10533-019-00555-8

Weisbrod, N., Dragila, M. I., Nachshon, U., & Pillersdorf, M. (2009). Falling through the cracks: The role of fractures in Earth-atmosphere gas exchange. *Geophysical Research Letters*, *36*(2), 1–5. https://doi.org/10.1029/2008GL036096

Werner, D., Grathwohl, P., & Höhener, P. (2004). Review of field methods for the determination of the tortuosity and effective gas-phase diffusivity in the vadose zone. *Vadose Zone Journal*, *3*(4), 1240–1248. https://doi.org/10.2136/vzj2004.1240

White, W. B. (2016). Science of caves and karst: A half century of progress. In *Geological Society of America Special Papers* (Vol. 516, pp. 19–33). Geological Society of America. https://doi.org/10.1130/2015.2516(03)

Wolf, B., Chen, W., Brüggemann, N., Zheng, X., Pumpanen, J., & Butterbach-Bahl, K. (2011). Applicability of the soil gradient method for estimating soil-atmosphere CO_2, CH_4, and N_2O fluxes for steppe soils in Inner Mongolia. *Journal of Plant Nutrition and Soil Science*, *174*(3), 359–372. https://doi.org/10.1002/jpln.201000150

Xiao, X., Kuang, X., Sauer, T. J., Heitman, J. L., & Horton, R. (2015). Bare soil carbon dioxide fluxes with time and depth determined by high-resolution gradient-based measurements and surface chambers. *Soil Science Society of America Journal*, *79*(4), 1073–1083. https://doi.org/10.2136/sssaj2015.02.0079

Xie, Y., Huang, F., Yang, H., & Yu, S. (2021). Role of anthropogenic sulfuric and nitric acids in carbonate weathering and associated carbon sink budget in a karst catchment (Guohua), Southwestern China. *Journal of Hydrology*, *599*(126287), 1–10. https://doi.org/10.1016/j.jhydrol.2021.126287

Yang, R., Liu, Z., Zeng, C., & Zhao, M. (2012). Response of epikarst hydrochemical changes to soil CO_2 and weather conditions at Chenqi, Puding, SW China. *Journal of Hydrology*, *468–469*, 151–158. https://doi.org/10.1016/j.jhydrol.2012.08.029

Yang, X., Fan, J., & Jones, S. B. (2018). Effect of soil texture on estimates of soil-column carbon dioxide flux comparing chamber and gradient methods. *Vadose Zone Journal*, *17*(180112), 1–9. https://doi.org/10.2136/vzj2018.05.0112

Zhao, R., Liu, Z., Dong, L., Zhang, Q., & Liu, C. (2021). The fates of CO_2 generated by H_2SO_4 and/or HNO_3 during the dissolution of carbonate and their influences on the karst-related carbon cycle. *Journal of Hydrology*, *597*(125746), 1–8. https://doi.org/10.1016/j.jhydrol.2020.125746

Zhao, R., Liu, Z., Huang, H., & Dong, L. (2019). Difference in the relationship between soil CO_2 concentration and the karst-related carbon cycle under different land use types in Southwest China. *Carbonates and Evaporites*, *34*(4), 1569–1581. https://doi.org/10.1007/s13146-019-00506-2